
Latent Swap Joint Diffusion for Long-Form Audio Generation

Yusheng Dai^{*1} Chenxi Wang^{*1} Chang Li¹ Chen Wang² Jun Du¹ Kewei Li¹
Ruoyu Wang¹ Jiefeng Ma¹ Lei Sun³ Jianqing Gao³

Abstract

Previous work on long-form audio generation using global-view diffusion or iterative generation demands significant training or inference costs. While recent advancements in multi-view joint diffusion for panoramic generation provide an efficient option, they struggle with spectrum generation with severe overlap distortions and high cross-view consistency costs. We initially explore this phenomenon through the connectivity inheritance of latent maps and uncover that averaging operations excessively smooth the high-frequency components of the latent map. To address these issues, we propose Swap Forward (SaFa), a frame-level latent swap framework that synchronizes multiple diffusions to produce a globally coherent long audio with more spectrum details in a forward-only manner. At its core, the bidirectional Self-Loop Latent Swap is applied between adjacent views, leveraging stepwise diffusion trajectory to adaptively enhance high-frequency components without disrupting low-frequency components. Furthermore, to ensure cross-view consistency, the unidirectional Reference-Guided Latent Swap is applied between the reference and the non-overlap regions of each subview during the early stages, providing centralized trajectory guidance. Quantitative and qualitative experiments demonstrate that SaFa significantly outperforms existing joint diffusion methods and even training-based long audio generation models. Moreover, we find that it also adapts well to panoramic generation, achieving comparable state-of-the-art performance with greater efficiency and model generalizability. Project page is available at <https://swapforward.github.io/>.

1. Introduction

Diffusion models learn to generate data by progressively adding noise to existing samples and subsequently reversing this process to recover the original data. (Ho et al., 2020; Song et al., 2020b). They originally achieved remarkable success in text-to-image (Ho et al., 2020; Song et al., 2020a;b) and have rapidly expanded into text-to-video (He et al., 2022; Kim et al., 2024a; Qiu et al., 2023; Wang et al., 2023) and text-to-audio (Evans et al., 2024a; Ghosal et al., 2023b; Huang et al., 2023a;b; Li et al., 2024; Liu et al., 2023b; 2024). One significant challenge in diffusion models is length extrapolation, which aims to generate varying lengths long-form output using diffusion models trained on constrained-length data.

Long-form soundscapes and background music are in high demand for ambiance enhancement in real-life applications (e.g., in-car audio, sleep aids) and digital products (e.g., movies, video games). Existing approaches to audio generation can be broadly categorized into Language Models (LMs) (Borsos et al., 2023; Copet et al., 2023; Kreuk et al., 2022) and Diffusion Models (DMs) (Evans et al., 2024a;b; Tan et al., 2024). For LMs, most works adopt autoregressive architectures, suffering from temporal causality constraints (Agostinelli et al., 2023; Borsos et al., 2023; Copet et al., 2023; Kreuk et al., 2022). For long-form audio generation, as duration extends, these models are observed to produce increasing accumulate errors, with more severe repetition issues. For DMs, most prior works (Ghosal et al., 2023a; Huang et al., 2023a; Liu et al., 2023a; Majumder et al., 2024) formulate audio generation as a 2D mel-spectrogram denoising process, typically constrained to 10-second durations. Although Make-An-Audio2 (Huang et al., 2023a) and Flexible DiT (Anonymous, 2024) allow variable-length generation, they show weak length exploration capability for longer duration. More recently, Stable Audio (Evans et al., 2024a;b) has been trained directly on long-form audio sequences, but it requires significant computational resources. Additionally, only a limited maximum window version is open-sourced, and it remains sensitive to text prompts. *On the other hand, taming pretrained audio generation models to produce seamless and coherent long-form audio in a training-free manner remains underexplored in audio generation (Polyak et al., 2024).*

^{*}Equal contribution ¹University of Science and Technology of China ²Tsinghua University ³iFlytek Research. Correspondence to: Jun Du <jundu@mail.ustc.cn>.

Table 1. Swap Forward demonstrates strong *generalization* (adapting to both spectrum and image generation, U-Net and DiT architectures, and fixed or flexible attention window sizes), *simplicity* (using two fundamental swap operators in a forward-only manner), and *efficiency* (a 3 ~ 4× reduction in subview number and 11 ~ 14× faster than SyncD) to generate seamless and coherent long-form latents.

Method	Spectrum Adaptation	Forward Only	Fixed Attention Window	DiT Adaptation	Guidance Method	Runtime(s)
MultiDiffusion	✗	✓	✓	✓	-	40.06
MAD	✗	✓	✗	✗	Self-Attention	41.82
SyncDiffusion	✗	✗	✓	✓	Gradient Descent	401.03
Swap Forward	✓	✓	✓	✓	Latent Swap	35.16

Joint diffusion in panorama generation is considered a potentially efficient solution. Specifically, a new joint diffusion process is optimized by synchronizing several diffusion processes to produce a globally coherent output. Prior work mainly focuses on two issues: *achieving smooth transitions between adjacent subviews and maintaining global cross-view consistency, e.g., color and style, in distant subviews*. As representative work (Bar-Tal et al., 2023; Jiménez, 2023), MultiDiffusion (MD) aims to achieve smooth transitions by applying step-wise averaging operation on the overlap regions of the denoised subviews. However, due to a lack of explicit guidance, this approach relies on a high overlap rate that suffering from low efficiency but still lead to global perception mismatches across subviews. As an advanced version of MD, Merge-Attention-Diffuse (MAD) (Quattrini et al., 2024) merges and splits subview latents around the self-attention layer, enabling global attention over the entire panorama. However, the merge operation increases the self-attention window length, forcing the model to handle longer token sequences and repetitive position problems. Thus, it is observed to lead to significant performance degradation in DiT architectures in Tab. 3 and in spectrum generation models trained on short-length clips in Fig. 6. SyncDiffusion (Lee et al., 2023) proposes a promising guidance approach to enhance the global coherence by minimizing perceptual similarity (LPIPS loss) (Zhang et al., 2018) between each subview and the reference image. However, the additional forward and backward propagation can significantly increase computation and time costs. Meanwhile, LPIPS loss is observed to be insensitive to *intermediate* denoised mel-spectrograms. *Consequently, there remains a lack of efficient and architecture-agnostic joint diffusion methods that can achieve global cross-view consistent in both audio and panorama generation.*

In early experiment, we apply the classical Joint Diffusion method, MultiDiffusion (Bar-Tal et al., 2023), to spectrum-based audio generation. *As shown in Fig.1, the generate spectrograms exhibit low time-frequency resolution and distortion in overlap regions, leading to visual blurriness and low-quality audio with monotonous tails.* This phenomenon is particularly evident in complex audio including more spectral details, e.g. soundscapes and concertos.

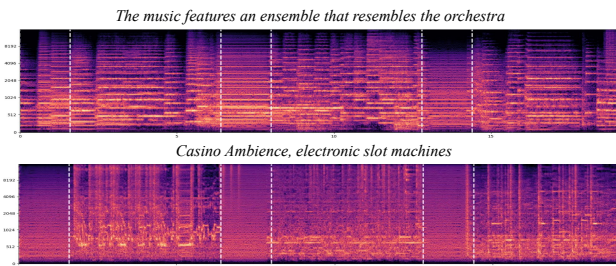


Figure 1. Mel-spectra generated by averaging operator based joint diffusion, e.g. MD (Bar-Tal et al., 2023). White narrow line areas represent overlapping regions that lack spectral details with monotonous tails.

To address these issue, in Section 2.2, we first investigate the causes of overlap distortion in spectra by existing joint diffusion. Specifically, we compare the differences between spectra and RGB images in their original features and identify the high-frequency variability inherent in mel-spectrograms. We then extend this analysis to the latent space through the connectivity inheritance of VAE latents. Through Fourier analysis, we uncover that the failure stems from the excessive suppression of high-frequency components caused by the latent averaging operator.

Based on these findings, in Section 2.3, we further reformulate the core of joint diffusion as a problem of merging step-wise differentiated trajectories. Leveraging the similarities and differences between these trajectories, we design Self-loop Latent Swap, a frame-level bidirectional latent swap operator applied to adjacent subviews. This operator adaptively enhances high-frequency details and mitigates latent aliasing in the overlapping region. To further achieve global cross-view coherence in the non-overlapping region, we propose Reference-Guided Latent Swap, a unidirectional latent swap operator that provides centralized trajectory guidance, efficiently enabling a global similarity-diversity trade-off in a forward-only manner.

Finally, in Section 3, we present extensive quantitative and qualitative experiments on long-form audio and panorama generation using both U-Net and DiT architectures. Compared to state-of-the-art (SOTA) joint diffusion methods and even other training-based approaches, SaFa is a simple yet efficient that achieves superior generation quality through only two fundamental swap operators across two tasks, en-

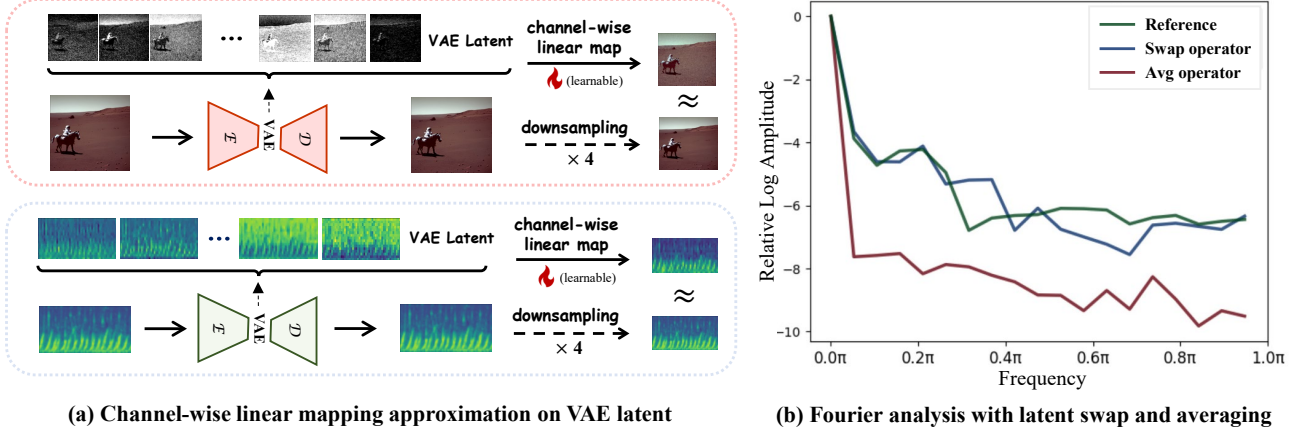


Figure 2. (a) The channel-wise linear mapping from original feature to its corresponding VAE latent ensures the connectivity inheritance, maintaining a similar frequency analysis pattern. (b) The relative log-amplitude curves of fourier analysis on non-overlapping regions (Reference) and overlapping regions of the denoised spectrum latent map with the latent averaging (Avg) and latent swap (Swap) operator.

ensuring better-blended transitions and enhanced global cross-view consistency without incurring additional costs. Further advantages of SaFa are demonstrated in Tab. 1.

2. Methodology

2.1. Joint Diffusion for Long Latent Generation

Diffusion models initially operate in the original feature space (Ho et al., 2020), but have recently been extended to the VAE latent space, achieving higher fidelity and compression rates (Rombach et al., 2022). From the perspective of Latent Diffusion Models (LDMs), most modality generation tasks (e.g. audio and image) can be effectively reformulated as latent generation problem (Liu et al., 2023a; Rombach et al., 2022). Considering a long latent generation based on a reference latent diffusion model Φ and conditions $\{y_i\}_{i=0}^n$, our target is to generate a 2D long latent map $J \in \mathbb{R}^{C \times H \times W}$ ($H \ll W$) through a joint diffusion process Ψ by merging a sequence of subview latent $\{X^i\}_{i=1}^n \in \mathbb{R}^{C \times H_x \times W_x}$. The subview mappings F_i , from overview J to subviews X_i ,

$$F_i \leftrightarrow R(F_i) : J \rightarrow X_i, i \in [n] \quad (1)$$

can be considered as a 1D sliding window process. Considering that in the spectrum $H \ll W$, we simplify the overlap mapping $I_{i,i+1}$ between adjacent subviews X_i and X_{i+1} as:

$$I_{i,i+1} \leftrightarrow R(F_i) \cap R(F_{i+1}) \quad (2)$$

and the non-overlap mapping $M_{i,i+1,i-1}$ of subview X_i as:

$$M_{i,i+1,i-1} \leftrightarrow R(F_i) - (R(F_{i-1}) \cup R(F_{i+1})) \quad (3)$$

For a joint diffusion step $\Psi(J_t | Y)$ at time-step t , most previous work (Bar-Tal et al., 2023; Jiménez, 2023; Lee et al., 2023) apply averaging operator to synchronize different

denoising trajectories in overlap regions,

$$\Psi(J_t | Y) = \sum_{i=1}^n \frac{F_i^{-1}(W_i)}{\sum_{j=1}^n F_j^{-1}(W_j)} \odot F_i^{-1}(\Phi(X_t^i | y_i)) \quad (4)$$

where W_i is the weight matrix, through averaging in overlapping regions and exclusivity in non-overlapping regions.

2.2. Comparative Analysis of Spectra and Image Latent

To address the overlap distortion problem in Fig. 1, we first conduct a comparative analysis of the VAE latent spaces for different modalities, a research area that has received limited prior investigation. Our main insight comes from the differences between the original features of the mel-spectrogram and RGB images. The mel-spectrogram is a 2D time-frequency representation of the audio signal, showing amplitude variability across frequency bands over time. Compared with RGB images, most mel-spectrograms show high-frequency variability, where amplitude values in time-frequency bins exhibit weak connectivity, characterized by sparsity and discreteness, without forming continuous contours as normal images. Further, in Fig. 2 (a), such discrepancy can extend to the VAE latent due to its connectivity inheritance via the channel-wise linear mapping with the original feature, which is first observed in image generation and has been served as a fast previewer to replace the VAE decoder¹. In this paper, we provide a formal formulation and extend it to spectrum generation. Specifically, given an image or spectrum $X \in \mathbb{R}^{C_x \times W_x \times H_x}$ and its VAE latent representation $Z \in \mathbb{R}^{C_z \times W_z \times H_z}$, a constant linear mapping $W \in \mathbb{R}^{C_x \times C_z}$ along the channel dimension satisfies

$$\text{Downsample}(X) \approx W \cdot Z \quad (5)$$

¹<https://discuss.huggingface.co/t/decoding-latents-to-rgb-without-upscaling/23204/2>

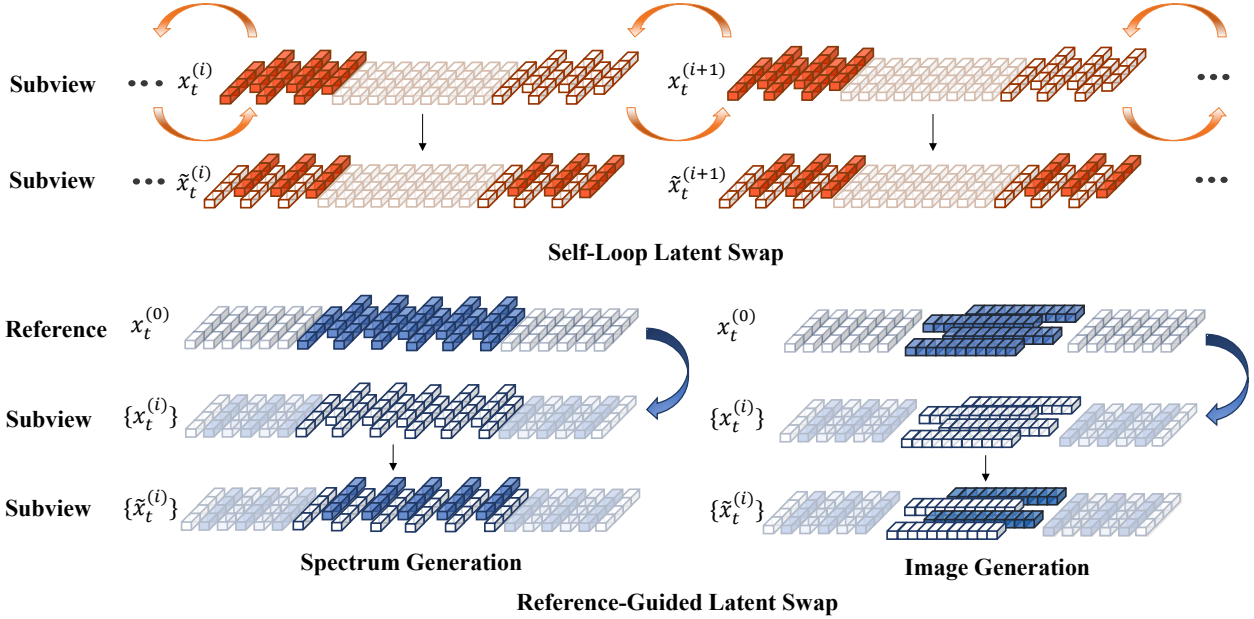


Figure 3. Self-Loop Swap is a synchronous, bidirectional latent swap operation that occurs in the overlap region at each denoising step. Reference-Guided Swap uses an independent reference denoising process to guide others through unidirectional latent swaps, ensuring global consistency across subviews.

Correspondingly, the inverse process can be described as:

$$Z \approx (W^T W)^{-1} W^T \cdot \text{Downsample}(X) \quad (6)$$

Such linear mapping along the dimension ensures that latent map inherits the connectivity and high-frequency variability of the original features, visually structural alignment.

In Fig. 2, we further demonstrate how the averaging operator affects the diffusion process of spectrum latents by comparing the relative log amplitude curves of non-overlap and overlap regions using Fourier frequency analysis. The Figure 2 (b) reveals that the weighted averaging operator excessively smooths the high-frequency components, causing a more pronounced decline, especially in the later stages of the process. This results in detail loss and distortion, manifesting visually as blurriness and audibly as monotonous tail sounds. However, when applying the averaging operator to image generation, the detail distortion is not as visually noticeable, as it is masked by the alignment low-frequency components terms of global contours and colors.

2.3. Latent Swap Joint Diffusion

Stepwise Differentiated Trajectories Building on the above findings, our target is to enhance high-frequency details while avoiding aliasing in latent map of overlap region. Focusing on the overlapping region, the essence of joint diffusion can be regarded as the merging of stepwise differentiated trajectories x_t^i and x_t^{i+1} that share the same previous-step initial overlapping latent $I_{i,i+1}(J_{t+1})$,

$$I_{i,i+1}(J_t) = W_i \odot \text{Right}(X_t^i) + (1 - W_i) \odot \text{Left}(X_t^{i+1}) \quad (7)$$

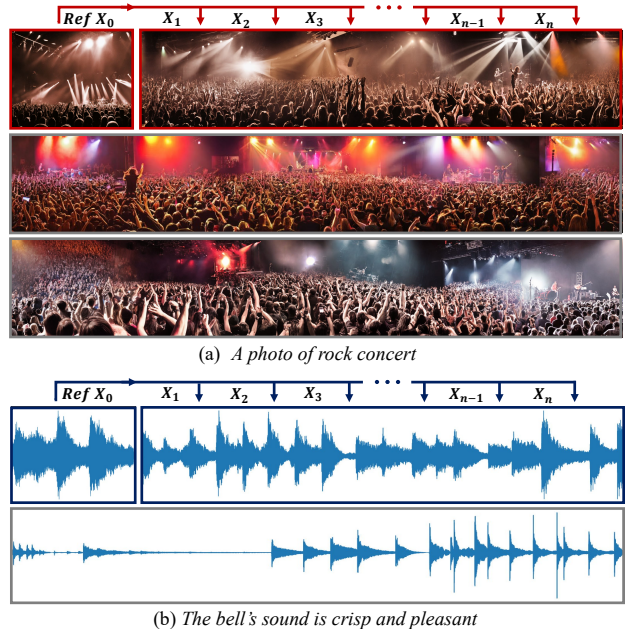


Figure 4. With Reference-Guided Swap, the panorama and waveform in the first row of subfigure (a) and subfigure (b) demonstrate enhanced global coherence (color and style for the image) and unified consistency (timbre and signal-to-noise ratio for audio), compared to the unguided results in the last row. By flattening the image into a 1D sequence, we apply the swap along the row axis to achieve segment-level swap, avoiding repetition and preserving diversity more effectively than the pixel-wise swap along the column axis, as shown in the middle row of subfigure (a).

where $\text{Left}(\cdot)$ and $\text{Right}(\cdot)$ represent subregion mapping functions for the left and right overlapping regions. Thus,



Figure 5. Reference-Guided Latent Swap achieves the cross-view similarity-diversity trade-off by the centralization reference trajectory guidance through unidirectional latent swap in early $r_{\text{guide}} \times T$ guidance steps.

these stepwise trajectories exhibit both differences—arising from latent influences outside the overlap and similarities—inherited from the shared initial state at the previous step, which can be formulated as:

$$0 < \varepsilon_l \leq d(\text{Right}[\Phi(F_i(J_{t+1}), y_i)], \text{Left}[\Phi(F_{i+1}(J_{t+1}), y_i)]) \leq \varepsilon_u < 1 \quad (8)$$

where the lower bound ε_l prevents complete similarity, the upper bound ε_u restricts excessive divergence, and $d(\cdot)$ is a distance metric.

Self-Loop Latent Swap Leveraging the properties of stepwise differentiated trajectories, we introduce the latent swap operator W_{swap} that consisting of binary elements 0 and 1, as a subset of the weight matrix W_i in Eq. 7. Compared to the averaging operator with constant matrix $W_{\text{avg}} = c \cdot \mathbf{1}_{m \times n}$, the binary swap operator samples and preserves the original denoised latent from x_t^i and x_t^{i+1} rather than smoothing with each other. The similarity of step-wise difference trajectory and the robustness of the diffusion model ensure controlled distribution to the joint diffusion trajectory. On the other hand, from a frequency analysis perspective, unlike the averaging operator, which acts as an all-pass filter, the latent swap operator functions as a band-pass filter, adaptively enhancing specific frequency components based on stepwise differential trajectory differences. By controlling the swap interval and swap direction, we can selectively enhance particular frequency bands. In this paper, we adopt a frame-level latent swap operator W_{swap} with swap interval m ,

$$W_{\text{swap}} = \mathbf{1}_n \otimes v_m, \quad v_m^{(i)} = \frac{1}{2} \left[1 - (-1)^{\lfloor \frac{i-1}{w} \rfloor} \right] \quad (9)$$

We choose the optimized swap interval $w = 1$, following the experimental details shown in Appendix 5.1. As delineated in Fig. 2 (c), we conduct Fourier frequency analysis

Algorithm 1 Latent Swap Joint Diffusion

Input: Reference model Φ , subview mapping $\{F_i\}_{i=0}^n$, conditions $\{y_i\}_{i=0}^n$, guidance step rate r_{refer} , region slice operations $\text{Right}(\cdot)$, $\text{Middle}(\cdot)$, and $\text{Left}(\cdot)$.

$J_T \sim P_{\mathcal{J}} \triangleright$ noise initialization

for $t \leftarrow T$ **to** 1 **do**

$X_t^i = \Phi(F_i(J_{t+1}), y_i), \forall i \in [0, n]$

\triangleright Eq. 7 Self-Loop Latent Swap

$I_{i,i+1}(J_t) = \text{Swap}(\text{Left}(X_t^{i+1}), \text{Right}(X_t^i)), \forall i \in [n]$

if $t \geq r_{\text{guide}} \times T$ **then**

\triangleright Eq. 10 Reference-Guided Latent Swap

$M_i(J_t) = \text{Swap}(\text{Middle}(X_t^0), \text{Middle}(X_t^i)), \forall i \in [n]$

Output : J_0

\triangleright the implement of frame-level latent swap

Function $\text{SWAP}(X_1, X_2)$:

$W_{\text{swap}} = \mathbf{1}_n \otimes v_m, v_m^{(i)} = \frac{1}{2} \left[1 - (-1)^{\lfloor \frac{i-1}{w} \rfloor} \right] \triangleright$ Eq.9

$X_{\text{new}} = W_{\text{swap}} \odot X_1 + (1 - W_{\text{swap}}) \odot X_2;$

Return : X_{new}

on the denoised latent from the overlapping region where the latent swap operation is applied. The result indicates that the latent swap operator shows the same trend as the reference curve from the non-overlapping region. This implies that the latent swap operation successfully enhances high-frequency components while minimizing disturbances to low-frequency components, thereby contributing to a superior output in terms of both fidelity and detail preservation in the overlap region. At a high level, the latent swap operation applied to the overlap region $I_{i,i+1}$ is performed sequentially across each subview (including between the first and last subviews), forming a loop swap process without central guidance. Hence, we name it *Self-Loop Latent Swap*. Moreover, we find the swap operation is also well adapted to panorama images generation, as shown in Fig. 4 and 6, achieving better-blended transitions and preserving more details.

Reference-Guided Latent Swap To mitigate cross-view inconsistency, Multidiffusion (Bar-Tal et al., 2023) adopts a small sliding window shift to avoid non-overlapping regions, which performs poorly due to the lack of explicit guidance and inefficiency with excessive redundant subview diffusion. SyncDiffusion (Lee et al., 2023) provides centralized guidance by optimizing initial subview denoising with LPIPS loss. However, it incurs nearly $10\times$ higher time cost, and the LPIPS loss is not compatible with the intermediate denoised mel-spectrogram. To address these issues, we propose the unidirectional *Reference-Guided Latent Swap*, designed to efficiently achieve global cross-view consistency in forward-only manner (e.g., timbre or SNR for audio, and style or color for images). Specifically, for the early $r_{\text{guide}} \times T$ of the denoising steps, we refine the non-overlapping trajectory

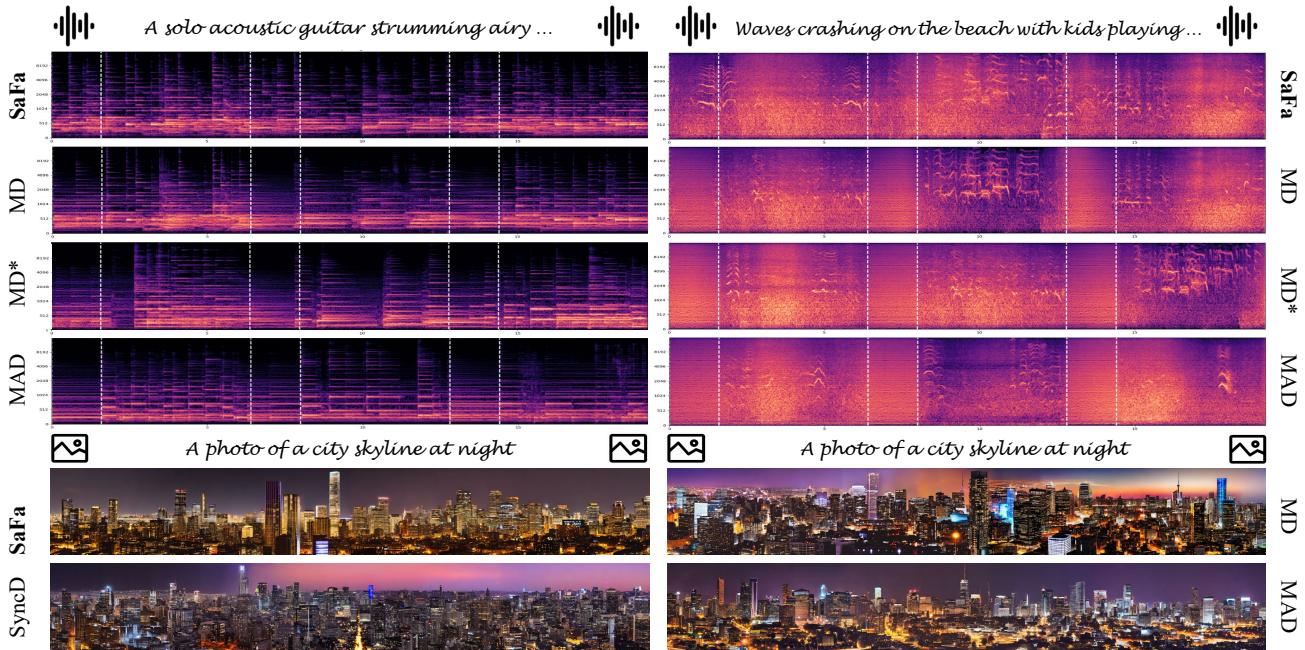


Figure 6. Qualitative comparisons. Top: In mel-spectrogram generation, SaFa demonstrates significantly better-blended transitions and preserves fine details in the overlap region (narrow white band) compared to other methods. Bottom: In panorama generation, MD (Bar-Tal et al., 2023) produces seamless outputs but exhibits global cross-view incoherence in color and style. In contrast, SaFa achieves comparable cross-view coherence and smooth transitions to MAD (Quattrini et al., 2024) and SyncD (Lee et al., 2023), without additional computational or time costs. From the global view, SaFa achieves a similarity-diversity trade-off in both audio and panorama generation.

$M_i(J_t)$ guided by the shared independent reference diffusion trajectory X_t^0 to achieve cross-view consistency with swap operator W_{refer} :

$$M_i(J_t) = W_{refer} \odot \text{Middle}(X_t^0) + (1 - W_{refer}) \odot \text{Middle}(X_t^i) \tag{10}$$

The Reference-Guided Latent Swap can be considered a frame-level blended diffusion (Avrahami et al., 2022b) process that guides the non-overlapping trajectory $M_i(J_t)$ to align with the reference trajectory x_t^0 , while maintaining coherence with nearby overlapping trajectories $I_{i-1,i}(J_t)$ and $I_{i,i+1}(J_t)$. For the later $(1 - r_{guide}) \times T$ of the denoising steps, similar to SDEdit (Meng et al., 2021), the non-overlapping trajectories start from the similar intermediate denoised latent maps to achieve cross-view consistency and avoid repetition simultaneously. By adjusting the swap timing (early $r_{guide} \times T$ stage) and the swap interval (w in Eq. 9), we can achieve a similarity-diversity trade-off for the global coherence. As shown in Fig. 5, we take panorama generation as an example for better visualization and we observe increased similarity but decreased diversity as r_{guide} increases. Additionally, excessive guidance after 60% of the late denoising steps has been observed to cause artifacts. As a result, we implement SaFa with $r_{guide} = 0.3$. More samples in audio generation are shown in Appendix Fig. 8. As for the swap interval, we follow the implementation in Eq. 9, adopting a frame-wise column swap with $w = 1$. For image generation, considering the flattening order in

the 1D token sequence², we adopt a row swap to achieve a segment-wise swap (Fig. 4 (a) line 1) instead of a pixel-level swap (Fig. 4 (a) line 2) in 1D token sequences, preventing excessive similarity.

3. Experiment

3.1. Long-Form Audio Generation

Baselines We compare our approach with other joint diffusion method in Tab. 2, including *MultiDiffusion* (MD) (Bar-Tal et al., 2023), an enhanced version *MultiDiffusion* (MD*) (Polyak et al., 2024) with the triangular window, and *Merge-Attend-Diffuse* (MAD) (Quattrini et al., 2024). SyncDiffusion (Lee et al., 2023) is not implemented on audio generation, since LPIPS loss is observed to be insensitive to *intermediate* denoised mel-spectrograms. Further, we compare SaFa with other training-based long audio generation models includes *AudioGen* (Kreuk et al., 2022), *Stable Diffusion Audio* (SD-audio) (Evans et al., 2024a) and *Make-An-Audio2* (Make2) (Huang et al., 2023a) on large-scale audio generation benchmark in Appendix 5.1.

Experiment Settings In Tab. 2, we implement all methods on two pretrained text-to-audio (TTA) models based on the AudioLDM (Liu et al., 2023a) framework. One adopts a

²Spectrograms are flattened first along the frequency axis, then along the time axis, while images follow the reverse order.

Table 2. Quantitative comparisons on audio generation (including soundscape, sound effect and music). In SaFa*, only Self-Loop Swap is applied. MD (Bar-Tal et al., 2023) uses averaging operation to represent equal contribution, while MD* (Polyak et al., 2024) uses a triangular function to represent a gradual transition to achieve better-blender coherence. Pink and purple blocks represent the best and second-best results, respectively.

Method	DiT						U-Net					
	FD↓	FAD↓	KL↓	CLAP↑	ILPIPS ↓	ICLAP↑	FD↓	FAD↓	KL↓	CLAP↑	ILPIPS ↓	ICLAP↑
Reference	2.92	0.22	0.74	0.54	0.39	0.86	4.12	0.27	1.15	0.53	0.43	0.79
MAD	12.77	7.56	0.86	0.51	0.32	0.93	16.33	8.12	1.25	0.49	0.36	0.88
MD	11.31	6.41	0.81	0.51	0.36	0.91	14.29	7.06	1.18	0.50	0.41	0.86
MD*	9.79	5.09	0.77	0.52	0.36	0.92	11.24	5.53	1.12	0.51	0.40	0.88
SaFa	6.84	4.91	0.73	0.54	0.34	0.95	7.88	4.27	1.11	0.53	0.36	0.92
SaFa*	6.98	4.89	0.73	0.54	0.36	0.94	7.58	4.14	1.12	0.54	0.39	0.90

masked DiT architecture (Gao et al., 2023), while the other uses AudioLDM’s original U-Net architecture. Both models incorporate a FLAN-T5 text encoder (Chung et al., 2024) and a pretrained 2D spectrum-based VAE model (Liu et al., 2023a), and are trained on the same dataset and pipeline with variable audio, music and speech clips during 0.32s to 10.24s following (Huang et al., 2023a). In inference stage, we use a DDIM sampler (Song et al., 2020a) with 200 denoising steps and a classifier-free guidance scale of 3.5. As for long-form generation, to simplify spectrum generation and facilitate user studies, we evaluate all the method to produce 24s looped audio at a 16kHz sample rate by combining three overlapping 10-second segments with a overlap rate $r_{overlap} = 0.2$. In SaFa, the Reference-Guided Latent Swap is applied during the initial 60 steps with $r_{guide} = 0.3$. Following (Quattrini et al., 2024), MAD is applied during the first 60 of 200 steps to achieve optimal results. Nine text prompts are used (three soundscape, three sound effect and three music), as listed in the first nine audio qualitative examples in Appendix 8.

Evaluation Metrics Following AudioLDM (Liu et al., 2023a), Frechet Distance (FD) and Frechet Audio Distance (FAD) are used for quality and fidelity estimation (similar to FID score in image generation), which are based on two audio classifier models PANNs (Kong et al., 2020) and VG-Gish (Hershey et al., 2017) respectively. KL divergence (KL) is also used at a pair level. Following previous work in panorama generation (Bar-Tal et al., 2023; Kim et al., 2024b; Lee et al., 2023), we first utilize the reference model to generate 500 10-seconds audio clips per prompt, obtaining the reference set. Since the objective metrics models are trained on 10-second clips, we sequentially extract 10-second segments from each long-form generated audio with a sliding window, obtaining multiple 500-sample evaluation subsets per prompt. Then we calculate FD, FAD, and KL scores between these subsets and the reference set, and the results are averaged to obtain the final score. As the reference, we also calculate these scores between two equal-sized

random splits of the reference set. For semantic alignment, CLAP score is applied (based on LAION-CLAP (Huang et al., 2023a; Wu et al., 2023)). Intra-LPIPS and Intra-CLAP (cosine similarity of audio CLAP embeddings) are used to estimate cross-view coherence by calculating internal similarity between 10s clips cropped from the slide window operation with overlap rate of 0.2. As a supplementary, FD, FAD, KL, and Intra-CLAP are calculated on audio signals, while Intra-LPIPS is based on the Mel-spectrum.

Quantitative Result As shown in Tab. 2, in both DiT and U-Net models, SaFa consistently outperforms other methods significantly in semantic alignment (CLAP) and generation quality (FD, FAD, and KL). SaFa approaches reference-level performance in CLAP and KL, demonstrating the latent swap operator’s superiority in enhancing time-frequency resolution and reducing confusion over the averaging operator. Compared to SaFa*, which only use Self-Loop Swap, SaFa achieves greater cross-view consistency (ILPIPS and ICLAP) through Reference-Guided Swap. MD* surpasses MD, consistent with (Polyak et al., 2024), but remains inferior to SaFa. MAD employs block-wise averaging operations, leading to further spectrum distortion with low quality. Additionally, it causes a position embedding repetition problem, resulting in monotonous and repetitive subviews with low ILPIPS score.

Qualitative Result and User Study In Fig.6, compared with MD, MD* and MAD, SaFa preserves more spectral details without distortion in the overlap on both U-Net and DiT architectures. More qualitative comparisons are provided in the Appendix 8. Furthermore, we conduct user studies on the generated audio samples to enhance evaluation reliability, collecting a total of 34 valid responses in which participants ranked generated samples based on audio quality, and global consistency e.g. style, timbre and SNR. The result aligns well with quantitative performance, showing a significant advantage for SaFa over other methods. The detail settings and results of user study are available in the Appendix 6 and Fig. 10.

Table 3. Quantitative comparison on panorama generation with the resolution of 512×3200 . In SaFa*, only Self-Loop Latent Swap is applied. KID and IStyleL values are scaled by 10^3 . Pink and purple blocks represent the best and second-best results, respectively.

Method	DiT (SD 3.5)						U-Net (SD 2.0)					
	FID↓	KID↓	CLIP↑	IStyleL↓	ILPIPS↓	Rtime↓	FID↓	KID↓	CLIP↑	IStyleL↓	ILPIPS↓	Rtime↓
Reference	28.19	0.01	32.57	5.49	0.60	-	33.37	0.01	31.60	8.72	0.73	-
MD	24.50	8.12	32.37	2.58	0.59	63.84	32.99	8.08	31.76	3.08	0.69	40.06
SyncD	24.25	8.07	32.36	2.54	0.57	668.46	44.58	19.98	31.84	1.42	0.55	401.03
MAD	65.10	55.73	31.79	0.67	0.47	65.93	48.25	28.14	32.11	1.94	0.59	41.82
SaFa	22.54	4.53	32.45	1.36	0.56	49.54	34.71	9.91	31.84	1.74	0.61	35.16
SaFa*	22.12	4.27	32.39	2.96	0.59	49.51	32.43	6.97	31.74	2.66	0.62	35.04

3.2. Panorama Generation

Experiment Settings We compare our method with MultiDiffusion (MD) (Bar-Tal et al., 2023), Merge-Attend-Diffuse (MAD) (Quattrini et al., 2024) and SyncDiffusion (SyncD) (Lee et al., 2023) on Stable Diffusion v2.0 (SD 2.0) with U-Net architecture (Rombach et al., 2022) and Stable Diffusion v3.5 with MMDiT architecture (SD 3.5), respectively. For SaFa, Reference-Guided Latent Swap is applied in the initial 15 steps with $r_{\text{guide}} = 0.3$. We utilize the same six prompts derived from the previous work (Bar-Tal et al., 2023; Lee et al., 2023; Quattrini et al., 2024) and each prompt generating 500 panorama images. The target panorama resolution is set to 512×3200 composed of subview images with a resolution of 512×640 . For other methods, following (Bar-Tal et al., 2023; Lee et al., 2023; Quattrini et al., 2024), the overlap rate of adjacent subviews r_{overlap} is set to 0.8, with a slide window stride of 128 pixels to obtain optimal performance. Specifically, for SaFa with explicit guidance in non-overlap region, we implement a much lower overlap rate $r_{\text{overlap}} = 0.2$ to achieve high efficiency while maintaining high quality. All experiments are conducted on a NVIDIA RTX A100 GPU.

Evaluation Metrics FID (Heusel et al., 2017) and KID (Bińkowski et al., 2018) is utilized to measure the fidelity and diversity. Using the reference model, we generate 500 images per prompt at a resolution of 512×512 to form the reference set. Correspondingly sized subview are cropped sequentially by a sliding window operation to obtain the evaluation datasets and then calculate scores between evaluation and reference dataset to obtain the final averaging result. As the reference, we also compute these scores between two equal random splits of the reference images. Intra-LPIPS (ILPIPS) (Zhang et al., 2018) and Intra-StyleL (IStyleL) (Gatys et al., 2016) assess internal consistency by dividing each panorama into five non-overlapping regions and randomly cropping one 512×512 subview from each. And we calculate these score across 10 pairwise combinations per image and average it on all samples to obtain the final score. As a reference, we use the reference dataset and randomly select 1,000 pairs to compute average ILPIPS and IStyleL. Mean CLIP score (CLIP) based on CLIP model

(Hessel et al., 2021) is used to evaluate semantic alignment. All results are averaged over six prompts. Time consumption is measured by Rtime, representing the total time to generate one panorama on the same NVIDIA RTX A100 GPU.

Quantitative Result In Tab. 3, compared to MD with averaging operator, SaFa* shows much better cross-view coherence (IStyleL, ILPIPS) and generation quality (FID, KID), highlighting the effectiveness of the latent swap operator in achieving smoother transitions and preserving detail in both mel-spectrogram and image generation. With Reference-Guided Swap, SaFa improves global coherence (IStyleL, ILPIPS) and ensures strong subview consistency. It also outperforms MAD and SyncD with lower FID and KID scores, indicating higher quality and smoother transitions. The ILPIPS gap with SyncD arises from its direct LPIPS-loss minimization in gradient descent. MAD performs significantly worse in DiT than U-Net due to its reliance on adapting the self-attention layer for long latent input. SD 3.5 struggles with length exploration due to its sole reliance on the transformer block and lack of convolutional layers in U-Net. In terms of time consumption, our method achieves the highest efficiency, being $11 \sim 14\times$ faster than SyncD.

Qualitative Result and User Study As shown in Fig. 6, MD produces seamless outputs but lacks color and style consistency. SaFa matches MAD and SyncD in global cross-view consistency and smooth transitions without extra computation or time costs. Furthermore, user studies confirm the quantitative results in generation quality and cross-view coherence. The result of user study Fig.11, setting details 6 and more qualitative results 8 are shown in Appendix.

4. Conclusion and Discussion

In this paper, we present Swap Forward (SaFa), a simple but efficient latent swap framework through two fundamental swap operators to generate seamless and coherence long-form audio generation. Compared to previous techniques, Swap Forward is more adaptable to various modality tasks (long audio and even panorama images) across different diffusion architectures. As a high-performance alternative to the averaging operation, this operator can be widely applied

in existing joint diffusion methods to achieve state-of-art performance without additional time and computational cost. As a point of discussion, while the latent swap operator is observed performs well in the 2D VAE latent spaces of spectra and images, several areas remain for exploration. For example, its practicality for 1D wav-based VAE latents or other discrete token-based representations like Residual Vector Quantization requires further investigation.

References

- Agostinelli, A., Denk, T. I., Borsos, Z., Engel, J., Verzetti, M., Caillon, A., Huang, Q., Jansen, A., Roberts, A., Tagliasacchi, M., et al. Musiclm: Generating music from text. *arXiv preprint arXiv:2301.11325*, 2023.
- Anonymous. FLEXOUNDIT: VARIABLE-LENGTH DIFFUSION TRANSFORMER FOR TEXT-TO-AUDIO GENERATION. In *Submitted to The Thirteenth International Conference on Learning Representations*, 2024. URL <https://openreview.net/forum?id=6Ty0yCCez>. under review.
- Avrahami, O., Lischinski, D., and Fried, O. Blended diffusion for text-driven editing of natural images. *2022 IEEE/CVF Conference on Computer Vision and Pattern Recognition (CVPR)*, pp. 18187–18197, 2021.
- Avrahami, O., Fried, O., and Lischinski, D. Blended latent diffusion. *ACM Transactions on Graphics (TOG)*, 42:1 – 11, 2022a.
- Avrahami, O., Lischinski, D., and Fried, O. Blended diffusion for text-driven editing of natural images. In *Proceedings of the IEEE/CVF conference on computer vision and pattern recognition*, pp. 18208–18218, 2022b.
- Bar-Tal, O., Yariv, L., Lipman, Y., and Dekel, T. Multidiffusion: Fusing diffusion paths for controlled image generation. In *International Conference on Machine Learning*, 2023.
- Bińkowski, M., Sutherland, D. J., Arbel, M., and Gretton, A. Demystifying mmd gans. *arXiv preprint arXiv:1801.01401*, 2018.
- Borsos, Z., Marinier, R., Vincent, D., Kharitonov, E., Pietquin, O., Sharifi, M., Roblek, D., Teboul, O., Grangier, D., Tagliasacchi, M., et al. Audioldm: a language modeling approach to audio generation. *IEEE/ACM transactions on audio, speech, and language processing*, 31:2523–2533, 2023.
- Brooks, T., Peebles, B., Holmes, C., DePue, W., Guo, Y., Jing, L., Schnurr, D., Taylor, J., Luhman, T., Luhman, E., Ng, C., Wang, R., and Ramesh, A. Video generation models as world simulators. *OpenReview*, 2024. URL <https://openai.com/research/video-generation-models-as-world-simulators>.
- Chen, Y., Liu, S., and Wang, X. Learning continuous image representation with local implicit image function. In *Proceedings of the IEEE/CVF conference on computer vision and pattern recognition*, pp. 8628–8638, 2021.
- Chung, H. W., Hou, L., Longpre, S., Zoph, B., Tay, Y., Fedus, W., Li, Y., Wang, X., Dehghani, M., Brahma, S., et al. Scaling instruction-finetuned language models. *Journal of Machine Learning Research*, 25(70):1–53, 2024.
- Copet, J., Kreuk, F., Gat, I., Remez, T., Kant, D., Synnaeve, G., Adi, Y., and Défossez, A. Simple and controllable music generation. In *Thirty-seventh Conference on Neural Information Processing Systems*, 2023.
- Dao, T., Fu, D., Ermon, S., Rudra, A., and Ré, C. Flashattention: Fast and memory-efficient exact attention with io-awareness. *Advances in Neural Information Processing Systems*, 35:16344–16359, 2022.
- Défossez, A., Copet, J., Synnaeve, G., and Adi, Y. High fidelity neural audio compression. *arXiv preprint arXiv:2210.13438*, 2022.
- Esser, P., Rombach, R., and Ommer, B. Taming transformers for high-resolution image synthesis. In *Proceedings of the IEEE/CVF conference on computer vision and pattern recognition*, pp. 12873–12883, 2021.
- Evans, Z., Carr, C., Taylor, J., Hawley, S. H., and Pons, J. Fast timing-conditioned latent audio diffusion. In *ICML 2024*, 2024a.
- Evans, Z., Parker, J. D., Carr, C., Zukowski, Z., Taylor, J., and Pons, J. Long-form music generation with latent diffusion. *arXiv preprint arXiv:2404.10301*, 2024b.
- Gao, S., Zhou, P., Cheng, M.-M., and Yan, S. Masked diffusion transformer is a strong image synthesizer. In *Proceedings of the IEEE/CVF International Conference on Computer Vision*, pp. 23164–23173, 2023.
- Gatys, L. A., Ecker, A. S., and Bethge, M. Image style transfer using convolutional neural networks. In *Proceedings of the IEEE conference on computer vision and pattern recognition*, pp. 2414–2423, 2016.
- Ghosal, D., Majumder, N., Mehrish, A., and Poria, S. Text-to-audio generation using instruction tuned llm and latent diffusion model. *arXiv preprint arXiv:2304.13731*, 2023a.
- Ghosal, D., Majumder, N., Mehrish, A., and Poria, S. Text-to-audio generation using instruction-tuned llm and latent diffusion model. *arXiv preprint arXiv:2304.13731*, 2023b.
- He, Y., Yang, T., Zhang, Y., Shan, Y., and Chen, Q. Latent video diffusion models for high-fidelity long video generation. *arXiv preprint arXiv:2211.13221*, 2022.
- Hershey, S., Chaudhuri, S., Ellis, D. P., Gemmeke, J. F., Jansen, A., Moore, R. C., Plakal, M., Platt, D., Saurous, R. A., Seybold, B., et al. Cnn architectures for large-scale audio classification. In *2017 IEEE international conference on acoustics, speech and signal processing (icassp)*, pp. 131–135. IEEE, 2017.
- Hessel, J., Holtzman, A., Forbes, M., Bras, R. L., and Choi, Y. Clip-score: A reference-free evaluation metric for image captioning. *arXiv preprint arXiv:2104.08718*, 2021.
- Heusel, M., Ramsauer, H., Unterthiner, T., Nessler, B., and Hochreiter, S. Gans trained by a two time-scale update rule converge to a local nash equilibrium. *Advances in neural information processing systems*, 30, 2017.

- Ho, J., Jain, A., and Abbeel, P. Denoising diffusion probabilistic models. *Advances in neural information processing systems*, 33:6840–6851, 2020.
- Huang, J.-B., Ren, Y., Huang, R., Yang, D., Ye, Z., Zhang, C., Liu, J., Yin, X., Ma, Z., and Zhao, Z. Make-an-audio 2: Temporal-enhanced text-to-audio generation. *ArXiv*, 2023a.
- Huang, Q., Park, D. S., Wang, T., Denk, T. I., Ly, A., Chen, N., Zhang, Z., Zhang, Z., Yu, J., Frank, C. H., Engel, J., Le, Q. V., Chan, W., and Han, W. Noise2music: Text-conditioned music generation with diffusion models. *ArXiv*, abs/2302.03917, 2023b. URL <https://api.semanticscholar.org/CorpusID:256662408>.
- Jiménez, Á. B. Mixture of diffusers for scene composition and high resolution image generation. *arXiv preprint arXiv:2302.02412*, 2023.
- Kim, C. D., Kim, B., Lee, H., and Kim, G. Audiocaps: Generating captions for audios in the wild. In *Proceedings of the 2019 Conference of the North American Chapter of the Association for Computational Linguistics: Human Language Technologies, Volume 1 (Long and Short Papers)*, pp. 119–132, 2019.
- Kim, J., Kang, J., Choi, J., and Han, B. Fifo-diffusion: Generating infinite videos from text without training. *arXiv preprint arXiv:2405.11473*, 2024a.
- Kim, Y., Jo, D., Jeon, H., Kim, T., Ahn, D., Kim, H., et al. Leveraging early-stage robustness in diffusion models for efficient and high-quality image synthesis. *Advances in Neural Information Processing Systems*, 36, 2024b.
- Kingma, D. P. and Welling, M. Auto-encoding variational bayes. In *2nd International Conference on Learning Representations, ICLR 2014*, 2014. URL <http://arxiv.org/abs/1312.6114>.
- Kong, Q., Cao, Y., Iqbal, T., Wang, Y., Wang, W., and Plumbley, M. D. Panns: Large-scale pretrained audio neural networks for audio pattern recognition. *IEEE/ACM Transactions on Audio, Speech, and Language Processing*, 28:2880–2894, 2020.
- Kreuk, F., Synnaeve, G., Polyak, A., Singer, U., Défossez, A., Copet, J., Parikh, D., Taigman, Y., and Adi, Y. Audiogen: Textually guided audio generation. *arXiv preprint arXiv:2209.15352*, 2022.
- Lee, Y., Kim, K., Kim, H., and Sung, M. Syncdiffusion: Coherent montage via synchronized joint diffusions. *Advances in Neural Information Processing Systems*, 36:50648–50660, 2023.
- Lefaudeux, B., Massa, F., Liskovich, D., Xiong, W., Caggiano, V., Naren, S., Xu, M., Hu, J., Tintore, M., Zhang, S., Labatut, P., Haziza, D., Wehrstedt, L., Reizenstein, J., and Sizov, G. xformers: A modular and hackable transformer modelling library. <https://github.com/facebookresearch/xformers>, 2022.
- Li, C., Wang, R., Liu, L., Du, J., Sun, Y., Guo, Z., Zhang, Z., and Jiang, Y. Quality-aware masked diffusion transformer for enhanced music generation. *arXiv preprint arXiv:2405.15863*, 2024.
- Liu, H., Chen, Z., Yuan, Y., Mei, X., Liu, X., Mandic, D., Wang, W., and Plumbley, M. D. Audioldm: Text-to-audio generation with latent diffusion models. *arXiv preprint arXiv:2301.12503*, 2023a.
- Liu, H., Chen, Z., Yuan, Y., Mei, X., Liu, X., Mandic, D. P., Wang, W., and Plumbley, M. . Audioldm: Text-to-audio generation with latent diffusion models. In *International Conference on Machine Learning*, 2023b. URL <https://api.semanticscholar.org/CorpusID:256390486>.
- Liu, H., Yuan, Y., Liu, X., Mei, X., Kong, Q., Tian, Q., Wang, Y., Wang, W., Wang, Y., and Plumbley, M. D. Audioldm 2: Learning holistic audio generation with self-supervised pretraining. *IEEE/ACM Transactions on Audio, Speech, and Language Processing*, 2024.
- Lu, Z., Wang, Z., Huang, D., Wu, C., Liu, X., Ouyang, W., and Bai, L. Fit: Flexible vision transformer for diffusion model. *arXiv preprint arXiv:2402.12376*, 2024.
- Majumder, N., Hung, C.-Y., Ghosal, D., Hsu, W.-N., Mihalcea, R., and Poria, S. Tango 2: Aligning diffusion-based text-to-audio generations through direct preference optimization. In *Proceedings of the 32nd ACM International Conference on Multimedia*, pp. 564–572, 2024.
- Meng, C., He, Y., Song, Y., Song, J., Wu, J., Zhu, J.-Y., and Ermon, S. Sdedit: Guided image synthesis and editing with stochastic differential equations. *arXiv preprint arXiv:2108.01073*, 2021.
- Peebles, W. and Xie, S. Scalable diffusion models with transformers. In *Proceedings of the IEEE/CVF International Conference on Computer Vision*, pp. 4195–4205, 2023.
- Podell, D., English, Z., Lacey, K., Blattmann, A., Dockhorn, T., Müller, J., Penna, J., and Rombach, R. Sdxl: Improving latent diffusion models for high-resolution image synthesis. *arXiv preprint arXiv:2307.01952*, 2023.
- Polyak, A., Zohar, A., Brown, A., Tjandra, A., Sinha, A., Lee, A., Vyas, A., Shi, B., Ma, C.-Y., Chuang, C.-Y., et al. Movie gen: A cast of media foundation models. *arXiv preprint arXiv:2410.13720*, 2024.
- Qiu, H., Xia, M., Zhang, Y., He, Y., Wang, X., Shan, Y., and Liu, Z. Freenoise: Tuning-free longer video diffusion via noise rescheduling. *arXiv preprint arXiv:2310.15169*, 2023.
- Quattrini, F., Pippi, V., Cascianelli, S., and Cucchiara, R. Merging and splitting diffusion paths for semantically coherent panoramas. In *ECCV*, 2024.
- Rombach, R., Blattmann, A., Lorenz, D., Esser, P., and Ommer, B. High-resolution image synthesis with latent diffusion models. In *Proceedings of the IEEE/CVF conference on computer vision and pattern recognition*, pp. 10684–10695, 2022.
- Song, J., Meng, C., and Ermon, S. Denoising diffusion implicit models. *arXiv preprint arXiv:2010.02502*, 2020a.
- Song, Y., Sohl-Dickstein, J., Kingma, D. P., Kumar, A., Ermon, S., and Poole, B. Score-based generative modeling through stochastic differential equations. *arXiv preprint arXiv:2011.13456*, 2020b.
- Tan, Z., Ma, X., Fang, G., and Wang, X. Litefocus: Accelerated diffusion inference for long audio synthesis. *arXiv preprint arXiv:2407.10468*, 2024.
- Tang, L., Jia, M., Wang, Q., Phoo, C. P., and Hariharan, B. Emergent correspondence from image diffusion. *Advances in Neural Information Processing Systems*, 36:1363–1389, 2023.

- Van Den Oord, A., Vinyals, O., et al. Neural discrete representation learning. *Advances in neural information processing systems*, 30, 2017.
- Wang, F.-Y., Chen, W., Song, G., Ye, H.-J., Liu, Y., and Li, H. Gen-l-video: Multi-text to long video generation via temporal co-denoising. *arXiv preprint arXiv:2305.18264*, 2023.
- Wu, Y., Chen, K., Zhang, T., Hui, Y., Berg-Kirkpatrick, T., and Dubnov, S. Large-scale contrastive language-audio pretraining with feature fusion and keyword-to-caption augmentation. In *ICASSP 2023-2023 IEEE International Conference on Acoustics, Speech and Signal Processing (ICASSP)*, pp. 1–5, 2023.
- Zhang, C., Wu, Q., Gambardella, C. C., Huang, X., Phung, D., Ouyang, W., and Cai, J. Taming stable diffusion for text to 360° panorama image generation. In *Proceedings of the IEEE/CVF Conference on Computer Vision and Pattern Recognition*, pp. 6347–6357, 2024.
- Zhang, Q., Song, J., Huang, X., Chen, Y., and Liu, M.-Y. Diffcollage: Parallel generation of large content with diffusion models. In *2023 IEEE/CVF Conference on Computer Vision and Pattern Recognition (CVPR)*, pp. 10188–10198. IEEE, 2023.
- Zhang, R., Isola, P., Efros, A. A., Shechtman, E., and Wang, O. The unreasonable effectiveness of deep features as a perceptual metric. In *Proceedings of the IEEE conference on computer vision and pattern recognition*, pp. 586–595, 2018.

5. More Quantitive Experiments

5.1. Long-Form Audio Generation

Comparison on Open-Source Checkpoint We further aim to use the open-source audio diffusion checkpoints to conduct quantitative comparison of the joint diffusion methods, although most of the models are limited in compatibility with joint diffusion methods. For example, AudioLDM (Liu et al., 2023a) and Tango (Ghosal et al., 2023a) are trained with a fixed 10.24 seconds window to generate fixed-length audio clips. During training, shorter audio clips are padded with zeros up to 10.24 seconds, resulting in outputs that end with silence. Consequently, for joint diffusion methods based on these two models that concatenate subview latent maps, sudden silence is often observed in the overlap regions. Stable Diffusion Audio is also trained on a fixed 96-second window size and can produce variable-length outputs by end-cutting, which is also challenging to adapt for joint diffusion methods. In comparison, similar to our training pipeline, Make-An-Audio2 is trained with variable-length audio without excessive padding. It splits samples into different buckets based on their length during training, and within each batch, samples are randomly selected from the same bucket. However, we still observe some anomalous behavior when applying Make-An-Audio2 with Joint Diffusion.

As shown in Fig. 7, when applying it with SaFa, although it achieves significantly better blending and generation quality compared to MD and MAD, short abrupt transitions are observed at the end of each overlap region. Through experiments, we identify two main causes for this issue: (1) The VAE latent map of Make-An-Audio2 is sensitive to the last token swap from last subview. To address this, we shift the tail-end overlap region a 5 tokens forward duration Self-loop Swap. (2) Its 1D VAE is less robust to averaging and swapping operations at the latent level compared to AudioLDM (Liu et al., 2023a). Moving the concatenation operation at t_0 from the latent layer on the mel-spectrogram level effectively resolves this issue. Then we fix these two bugs, and it works well in SaFa+ as show in Fig. 7.

Comparison with Training-Based Methods We further compare our method with more extensive training-based long audio generation models, including both diffusion models and language models. While comparing absolute performance between models trained on different datasets and with varying model sizes is not meaningful, the relative performance degradation on each model with increasing audio generation length can highlight the strengths and weaknesses of these methods.

The training-based baselines include: (1) **AudioGen** (AuGen) (Kreuk et al., 2022) : An autoregressive model based on learned discrete audio representations, supporting ultra-

Table 4. Quantitative comparisons of join diffusion on 24-seconds audio generation on Make-An-Audio2 (Huang et al., 2023a).

Method	FD↓	FAD↓	KL↓	mCLAP↑
Make2	18.01	2.01	1.49	0.50
MD	65.28	17.70	3.22	0.24
MAD	62.53	16.88	3.05	0.26
SaFa	15.36	1.32	1.27	0.57

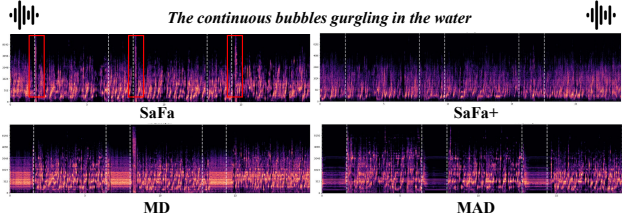


Figure 7. The 1D-VAE latent of Make-An-Audio2 is observed to be sensitive to the averaging operation in MD and MAD. The swap operation improves the situation significantly, but the swapped last token still causes abrupt transitions. In SaFa+, we address this issue by shifting the swap region forward by a few tokens.

Table 5. Quantitative Comparison with Training-Based Variable Length Audio Generation Models..

Method	FD↓	FAD↓	KL↓	mCLAP↑
SD-audio (10s)	38.23	6.20	2.19	0.40
SD-audio (32s)	25.52	6.43	2.24	0.37
SD-audio (64s)	25.82	6.12	2.25	0.35
SD-audio (96s)	30.11	6.54	2.38	0.33
AuGen (10s)	16.88	4.36	1.52	0.55
AuGen (32s)	18.54	4.81	1.71	0.50
AuGen (64s)	19.53	5.02	1.76	0.50
AuGen (96s)	18.88	5.44	1.78	0.49
Make2 (10s)	14.37	1.12	1.28	0.57
Make2 (27s)	18.49	2.26	1.55	0.49
SaFa (32s)	15.21	1.45	1.25	0.57
SaFa (64s)	15.14	1.25	1.24	0.57
SaFa (96s)	15.36	1.33	1.25	0.57

long audio generation. (2) **Stable Diffusion Audio** (SD-audio) (Evans et al., 2024a): A diffusion model trained on a fixed 96-second window size (the open-source checkpoint supports up to 47 seconds) and capable of producing variable-length outputs through end-cutting. (3) **Make-An-Audio2** (Make2) (Huang et al., 2023a): A diffusion model trained on variable-length window sizes with audio lengths from 0 to 20s. It can only support lengths of up to 27 seconds due to the maximum length of learnable positional encoding limit. For SaFa, we implement it on Make-An-Audio2 for a clearer comparison, maintaining the same settings as in Section 3.1.

We evaluate these four methods using the AudioCaps test set (Kim et al., 2019), which includes 880 ground truth samples collected from YouTube videos. The target generation

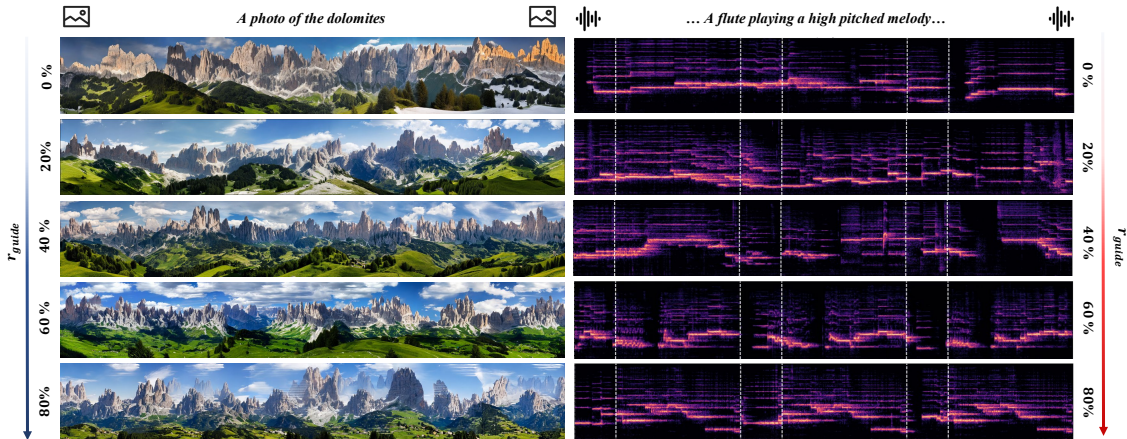


Figure 8. The effect of the trajectory guidance rate r_{guide} in Reference-Guided Swap on long spectrum and panorama generation.

Table 6. Length adaptation of SaFa on panorama generation.

Method	CLIP \uparrow	FID \downarrow	KID \downarrow	ILPIPS \downarrow	IStyleL \downarrow
SaFa (1600)	31.88	34.47	9.71	0.59	1.67
SaFa (3200)	31.84	34.71	9.91	0.61	1.74
SaFa (4800)	31.88	34.97	10.68	0.62	1.78

lengths are set to 32, 64, and 96 seconds. For SaFa, these outputs are concatenated from 4, 8, and 12 audio clips of 10 seconds, respectively. As in Section 3.1, we use FD, FAD, KL, and mCLAP to evaluate the generation quality and semantic alignment of the generated audio. A 10s sliding window with an 8s step size is used to generate the 10-second clips for evaluation, and the results are averaged to obtain the final scores.

As shown in Table 5, Make2, the state-of-the-art model for audio generation, demonstrates excellent performance in generating 10-second audio clips. However, it shows significant performance degradation when generating its maximum-length output of 27 seconds, as most training audio clips are under 20 seconds, and the model lacks specific design elements to generalize to longer unseen lengths. In contrast, our SaFa (32s) method, applied to Make2, maintains high performance in terms of FAD and mCLAP, with only minor degradation observed in FAD and KL compared to the Make2 (10s). Moreover, SaFa consistently delivers strong performance for 32-, 64-, and 96-second generation tasks without observable degradation. As for AuGen, although its architecture is inherently suited for generating longer audio compared to diffusion models, its performance degrades significantly as the generation length increases from 10 seconds to 96 seconds, accompanied by substantial increases in memory and time costs. Notably, its FAD score drops by 1.08, and its mCLAP score decreases by 0.06. In contrast, our method exhibits only a minor reduction in FAD of 0.03, while maintaining a stable mCLAP score. For SD-audio, improved FD performance is observed when increasing the generation length from 10 to 32 seconds,

likely due to the majority of its training data being focused on longer durations. However, other metrics consistently decline from 10 to 96 seconds, though the degradation is less pronounced compared to AuGen. This highlights the robustness of diffusion models in generating longer outputs within their maximum training window.

Length Adaptation As shown in Fig. 7, SaFa maintains strong, stable performance across all evaluated metrics for outputs of varying lengths of 24s, 48s and 72s, demonstrating the algorithm’s scalability to longer durations.

Effect of Guidance Steps and Swap Interval In Fig. 8, we further demonstrate the progressive transition from cross-view diversity to similarity by varying r_{guide} in both mel-spectrum and panorama generation using Reference-Guided Latent Swap. All other settings for SaFa remain consistent with Section 3. As shown in Fig. 8, using an appropriate trajectory guidance rate r_{guide} , e.g., 20% to 40%, results in unified cross-view coherence while preserving the diversity of local subviews. However, as the guidance rate r_{guide} increases beyond 60%, excessive repetition and artifacts begin to appear. This occurs because Reference-Guided Swap is a unidirectional operation, where the denoising process of the reference view is independent and unaffected by each subview. Consequently, it does not adapt as seamlessly to subviews in the later stages as the bidirectional Self-Loop Swap does. This is also one of the reasons why we restrict Reference-Guided Swap to the early denoising stages.

To further explore the effects of the swap interval w (in Eq. 9), we apply the Self-Loop Latent Swap with various w values in spectrum generation, as shown in Fig. 5.1. We observe that using a small swap interval (e.g., 1 or 2), corresponding to higher swap frequencies, produces smoother transitions. Conversely, larger w values indicate larger swap units, resulting in less seamless transitions between subviews. This outcome aligns with the high-frequency variability of mel tokens, leading us to default the Self-Loop

Table 7. Quantitative performance on length adaptation of SaFa on audio generation with DiT and U-Net architectures.

Method	DiT						U-Net					
	FD↓	FAD↓	CLAP↑	KL↓	ILPIPS ↓	ICLAP↑	FD↓	FAD↓	CLAP↑	KL↓	ILPIPS ↓	ICLAP↑
SaFa (24s)	6.84	4.91	0.54	0.73	0.34	0.95	7.88	4.27	0.53	1.11	0.36	0.92
SaFa (48s)	6.94	4.97	0.54	0.73	0.35	0.94	7.61	4.10	0.54	1.08	0.37	0.88
SaFa (72s)	6.98	4.99	0.54	0.72	0.35	0.93	7.68	4.21	0.53	1.13	0.37	0.89

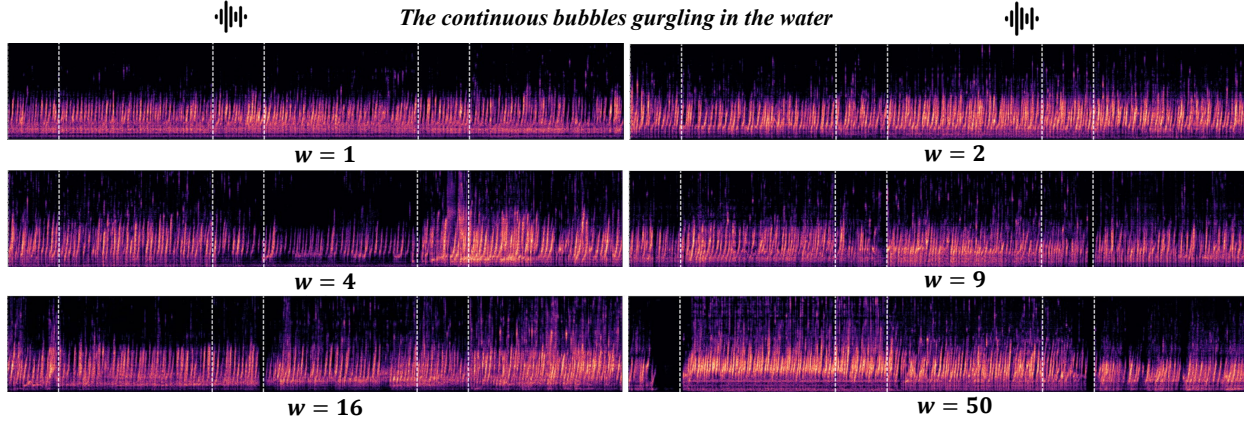


Figure 9. The effect of the swap interval w (in Eq.9) of Self-Loop Latent Swap on spectrum generation. Better transition is achieved with lower values of w , e.g., 1 or 2, which indicate a high swap frequency between two step-wise differential trajectories to enhance the high-frequency component in the denoised mel-spectrum.

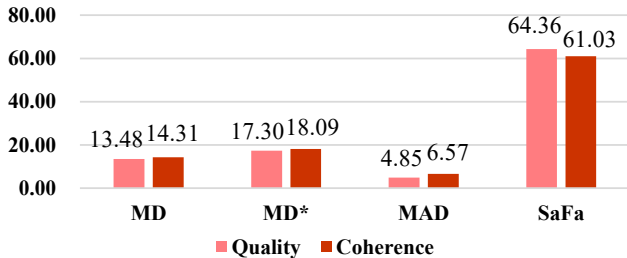


Figure 10. User study results on audio generation.

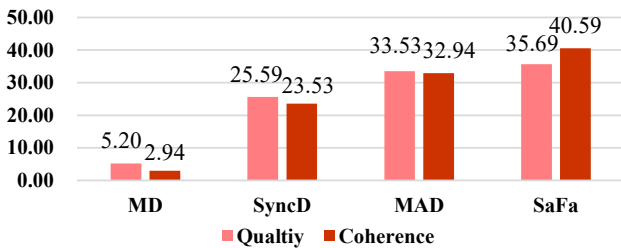


Figure 11. User study results on panorama generation.

Latent Swap to frame-level operations with $w = 1$ for optimal performance.

5.2. Panorama Generation

Length Adaptation In Tab.6, We utilize SD 2.0 model to estimate performance of SaFa on panorama images with resolutions of 512×1600 , 512×3200 , and 512×4800 . As a result, SaFa maintains stable and great performance across all evaluated metrics in different length output.

6. User Study

For subjective evaluation, we randomly select samples from the qualitative results of the top four methods in audio and panorama generation for user studies. We use the same notation as in Section 3.1. Specifically, SaFa is compared with MD, MD*, and MAD for audio generation, while for panorama generation, SaFa is compared with MD, MAD, and SyncD. For each task, we randomly select 30 parallel comparison groups (plus 2 additional pairs as a vigilance

group) from the four compared methods, evenly distributed across six prompts. We recruit 39 participants with basic machine learning knowledge but no prior familiarity with the research presented in this paper. Each participant is required to select the best sample from each of the 32 groups based on two evaluation dimensions: generation quality and global coherence. Semantic alignment is not considered, as most samples align well with the prompts semantically and cannot be easily distinguished in this regard. We ultimately collect 34 valid responses out of 39 participants. The results indicate that SaFa consistently outperforms the baseline methods, achieving superior human preference scores across both evaluation dimensions. Fig. 10 highlight the significant preference of human evaluators for SaFa in both quality and coherence assessments of audio generation. This preference stems from the swap operator’s enhanced adaptability to the inherent characteristics of spectral data, which lacks the typical global structural features or contours present in images. Meanwhile in Fig. 11, with significantly faster inference speeds and relying solely on fixed self-attention windows, SaFa achieves comparable performance to SyncD and MAD

in the subjective evaluation of panorama generation.

7. Related Works

7.1. Latent Diffusion Models

A key factor of diffusion models’s success is to applied effective learned representations across diverse data types. Extensive research has explored self-supervised learning to develop either discrete tokenizers (Défossez et al., 2022; Van Den Oord et al., 2017) or continuous distributions (Chen et al., 2021; Kingma & Welling, 2014). Among these, Variational Autoencoders (VAEs) (Kingma & Welling, 2014) provide a regularized, compressed latent space that accelerates training and inference while enabling high-quality generation. Recent work has applied VAE latent spaces across various generation tasks and modalities (Brooks et al., 2024; Evans et al., 2024a; Rombach et al., 2022), covering 2D image-based VAEs (Podell et al., 2023; Rombach et al., 2022) and 1D/2D mel-spectrogram representations (Evans et al., 2024a; Liu et al., 2023b). However, few studies have examined the unique characteristics and commonalities of these heterogeneous representations. In this paper, we aim to capture the distinctions between VAE representations based on their original data distributions (RGB pixel space and mel time-frequency space). We introduce a spectrum-inspired operator and surprisingly find it works well in recorrsponding VAE representations to pervese spectrum details without confuse. And it can even extend to image VAE latents due to the redundancy of representations and the robustness of the diffusion model. Text-guided diffusion models have shown remarkable performance across a wide range of applications, including image generation (Peebles & Xie, 2023; Rombach et al., 2022), video generation (Brooks et al., 2024; He et al., 2022), and audio generation (Evans et al., 2024a; Liu et al., 2023b). A key factor in this success lies in effectively learning representations across diverse data types. Extensive research has focused on self-supervised learning to develop either discrete tokenizers (Défossez et al., 2022; Van Den Oord et al., 2017) or continuous distributions (Chen et al., 2021; Kingma & Welling, 2014). Among these, Variational Autoencoders (VAEs) (Kingma & Welling, 2014) offer a regularized, compressed latent space that not only accelerates training and inference but also enables the generation of high-quality outputs. In recent years, numerous generation tasks across different modalities have leveraged the VAE latent space (Brooks et al., 2024; Evans et al., 2024a; Rombach et al., 2022), spanning general image-based 2D VAEs (Podell et al., 2023; Rombach et al., 2022) and 1D/2D mel-spectrogram representations (Evans et al., 2024a; Liu et al., 2023b). However, limited research has delved into the unique features and commonalities of these heterogeneous representations and data types. In this paper, we analyze the distinctions between VAE representations on RBD pix-

els and mel time-frequency bins within a multi-view joint diffusion framework for long-form latent generation. We propose a modality-agnostic latent swap operation as an alternative to the averaging operation, achieving smooth transition while preserving detail in overlapping regions.

7.2. Long-Form Audio Generation

In long-form generation of audio, the related work can be divided into Language Models (LMs) (Agostinelli et al., 2023; Borsos et al., 2023; Copet et al., 2023) and Diffusion Models (DMs) (Evans et al., 2024a;b; Tan et al., 2024). For LMs, most of them adapt autoregressive architectures that are limited by temporal causal characteristics. This leads to issues such as gradient accumulation, an inability to generate looped outputs, and significant resource consumption (Agostinelli et al., 2023; Borsos et al., 2023; Copet et al., 2023; Kreuk et al., 2022). Despite some proposed acceleration methods (Dao et al., 2022; Lefaudeux et al., 2022), quality challenges persist. For DMs, Stable Audio (Evans et al., 2024a) trains directly on long-duration data, requiring considerable resources and incurring high inference costs. Although we note potential solutions from other fields with FIFO algorithm (Kim et al., 2024a) and 2DRoPE (Lu et al., 2024), these methods still faces above challenges. The exploration of joint diffusion generation in audio generation remains limited (Polyak et al., 2024), and its applicability has yet to be established.

7.3. Panorama Generation

As the supplement, we further introduce some additional training-free and training-based methods for panorama generation. Early training-free research (Avrahami et al., 2021; 2022a; Esser et al., 2021) primarily relied on inpainting or outpainting techniques to produce seamless outputs. However, these methods often exhibit some repetition and are constrained by temporal causality (Lee et al., 2023; Quatrini et al., 2024). Recent advancements fine-tune stable diffusion models on 360-degree panorama datasets, yielding high-quality results but typically limited to specific themes (Tang et al., 2023; Zhang et al., 2024). Other methods introduce refined positional encodings adapted for varying inference lengths, while the model is required to be trained from scratch (Lu et al., 2024). In contrast, multiview joint diffusion (Bar-Tal et al., 2023; Zhang et al., 2023) performs parallel subview generation, efficiently combining them to obtain the final output without further fine-tuning. Therefore, we focus on further improving and extending joint diffusion in this paper.

8. Further Qualitative Comparison

More qualitative results on the audio generation are in Fig. 12 to 20 and panorama generation are in Fig. 21 to 31.

Casino Ambience, electronic slot machines

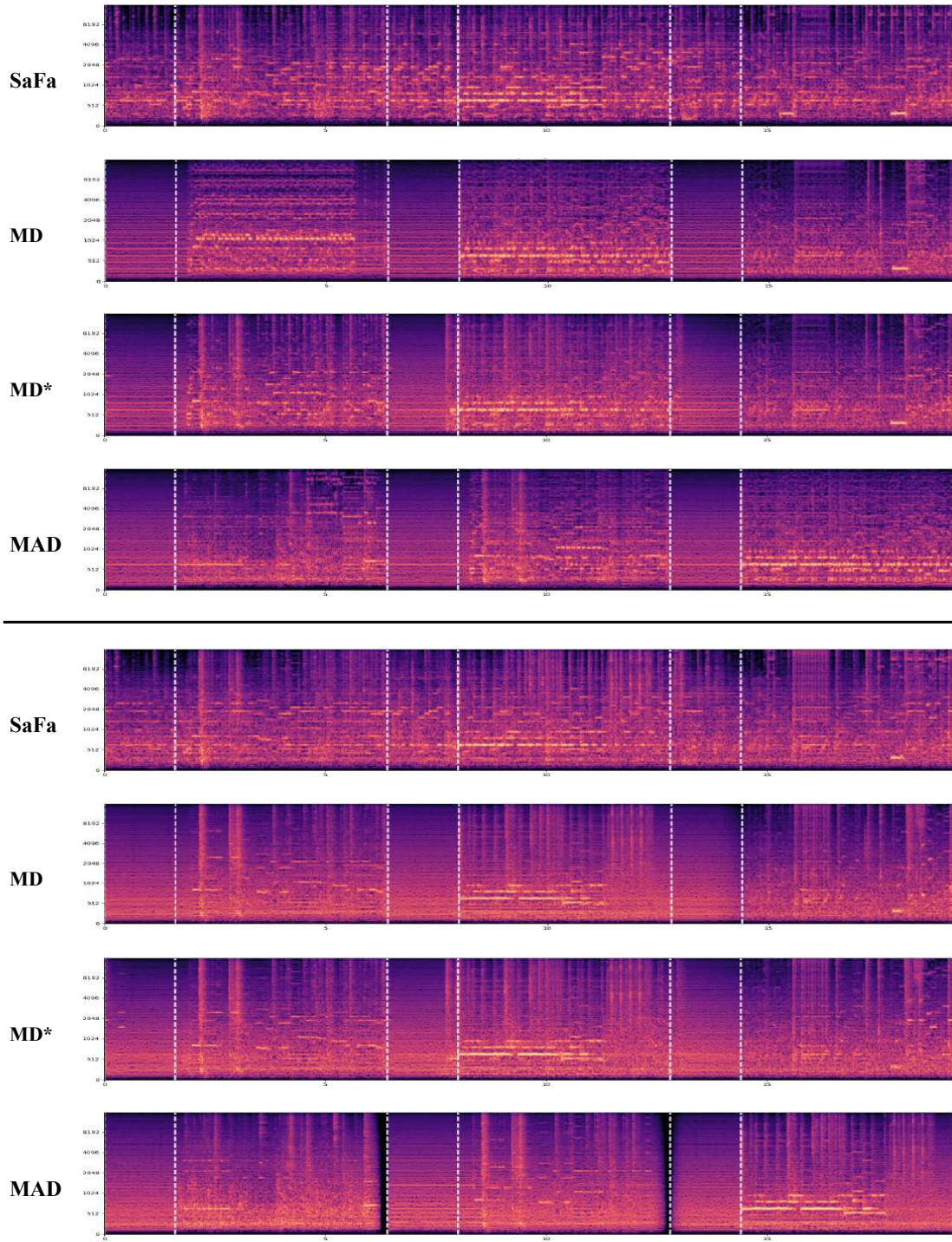


Figure 12. Qualitative comparison on soundscape generation. MD* represent an enhanced MD method with triangular windows.

Waves crashing on the beach with kids playing and seagull chirping

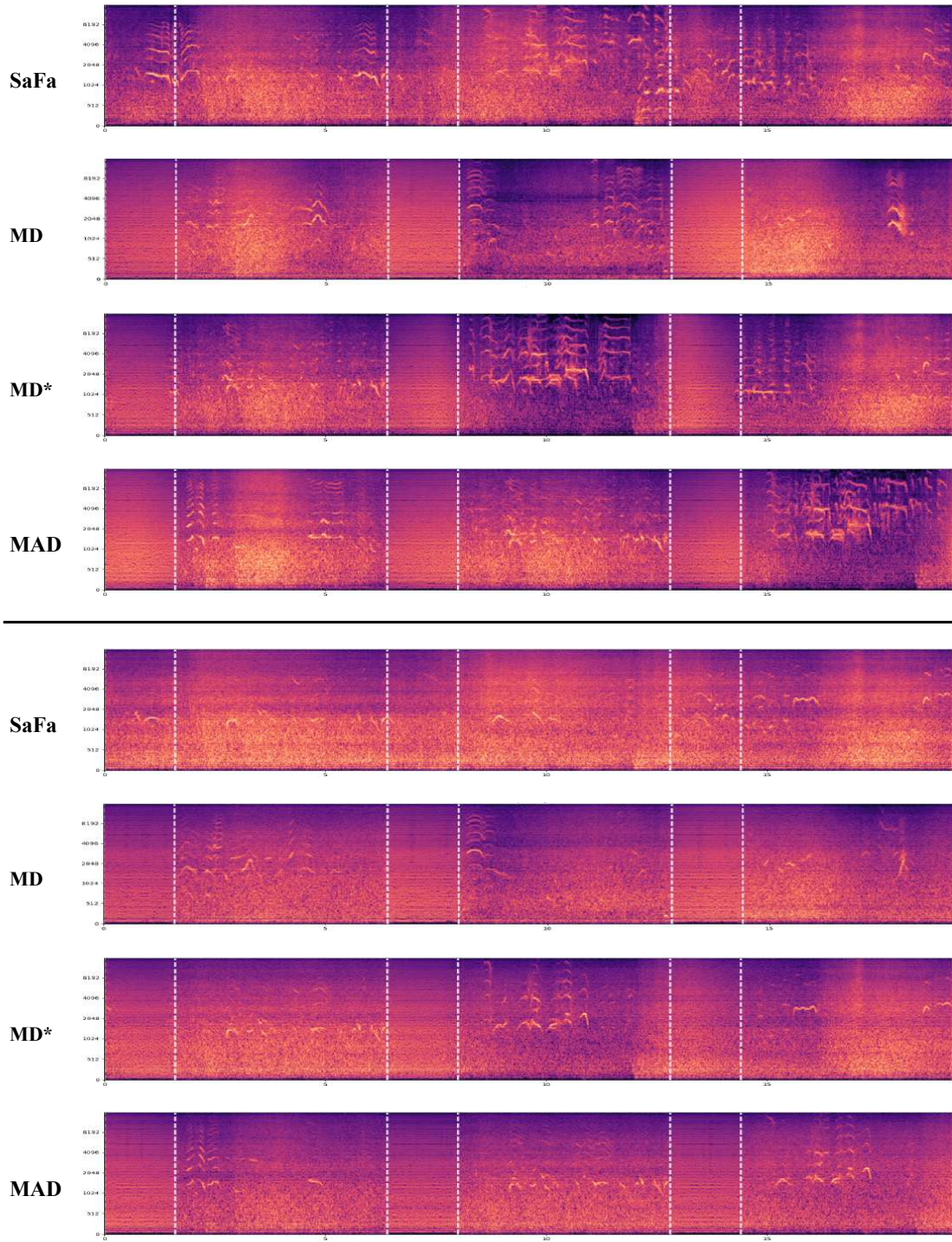


Figure 13. Qualitative comparison on soundscape generation. MD* represent an enhanced MD method with triangular windows.

The audience's enthusiastic and passionate cheers and loud whistles in the stadium

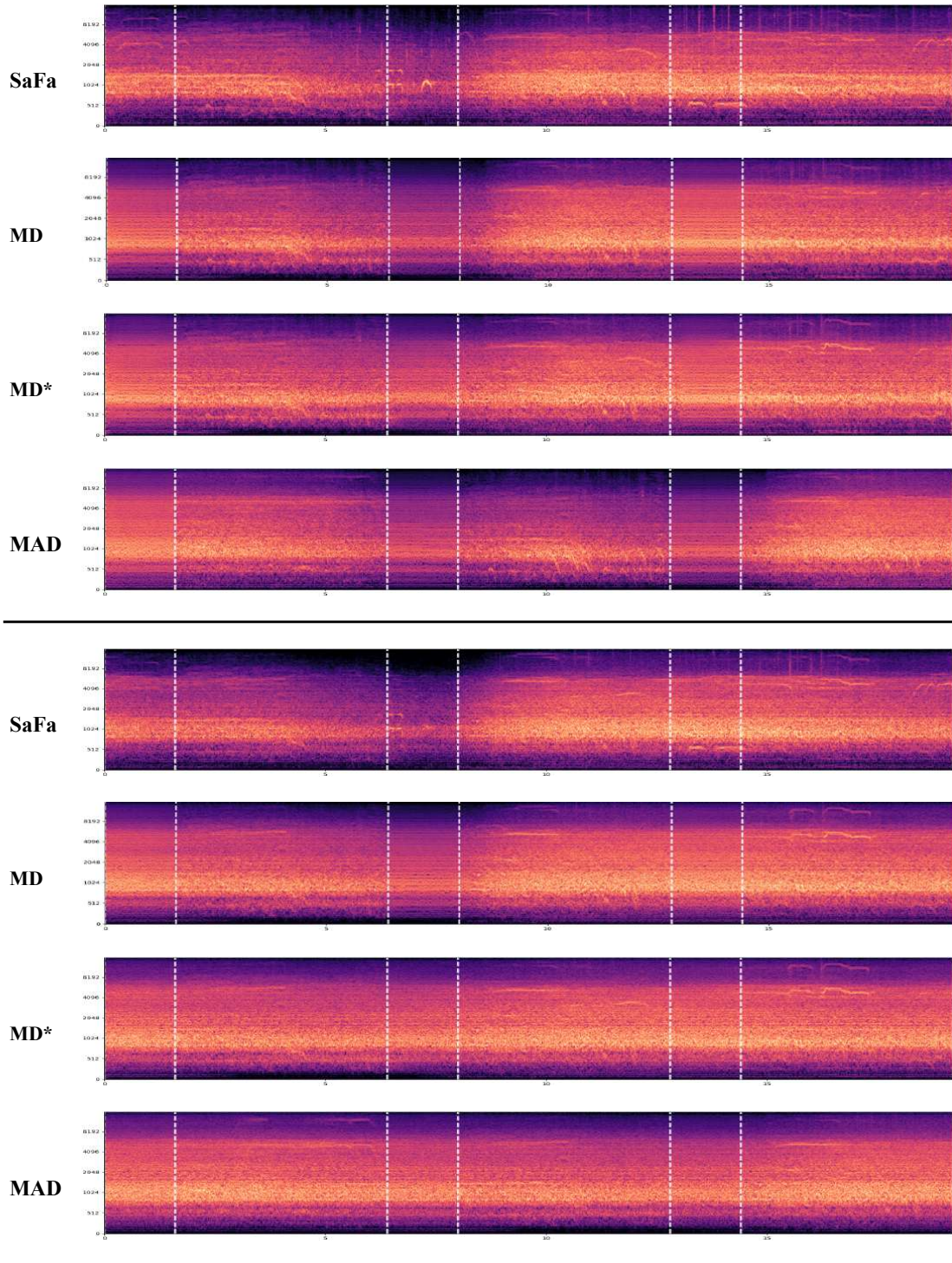


Figure 14. Qualitative comparison on soundscape generation. MD* represent an enhanced MD method with triangular windows.

Low fidelity audio from a live performance featuring a solo direct input acoustic guitar strumming airy, suspended open chords. Also present are occasional ambient sounds, perhaps papers being shuffled.

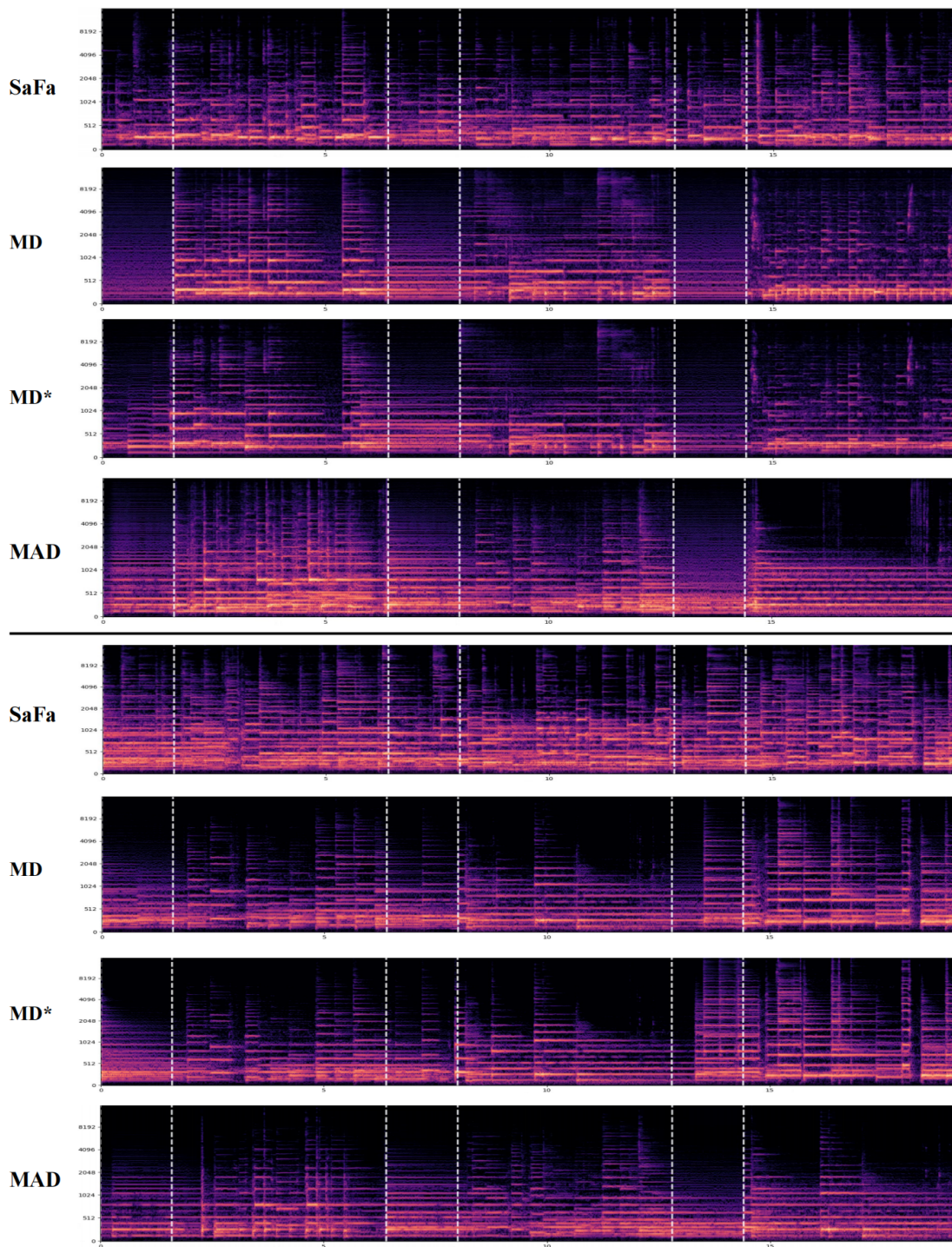


Figure 15. Qualitative comparison on music generation. MD* represent an enhanced MD method with triangular windows.

The instrumental music features an ensemble that resembles the orchestra. The melody is being played by a brass section while strings provide harmonic accompaniment. At the end of the music excerpt one can hear a double bass playing a long note and then a percussive noise.

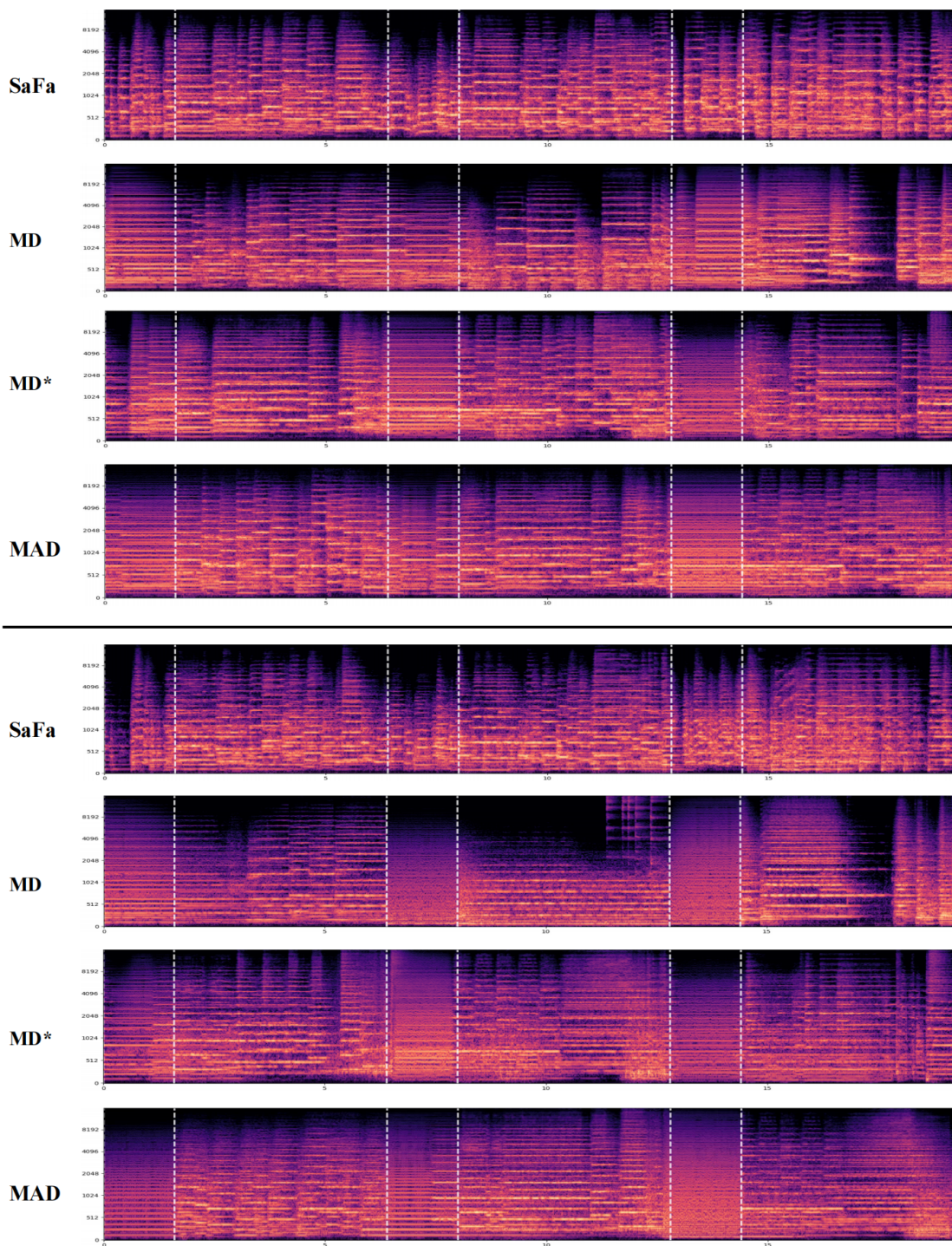


Figure 16. Qualitative comparison on music generation. MD* represent an enhanced MD method with triangular windows.

This instrumental song features a flute playing a high pitched melody. The melody starts off with one high pitched staccato note. After a brief pause, the flute plays two ascending notes in which the second note is sustained. Then a third higher note is played followed by a descending run of four more notes and ending on one higher note. There are no other instruments in this song. There is no percussion in this song. This song has a relaxing mood. This song can be played at a meditation center.

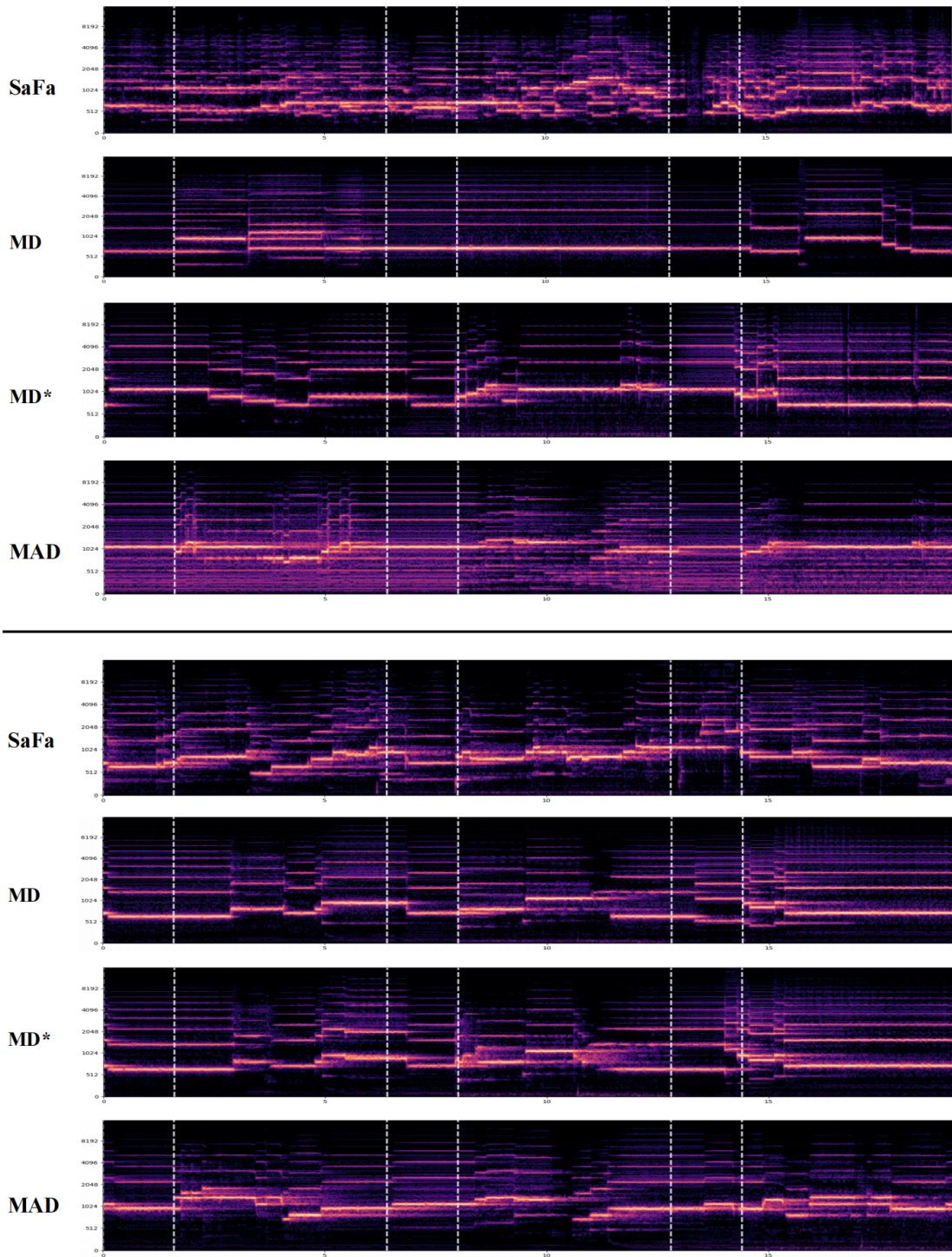


Figure 17. Qualitative comparison on music generation. MD* represent an enhanced MD method with triangular windows.

The continuous gurgling sound of bubbles in the water

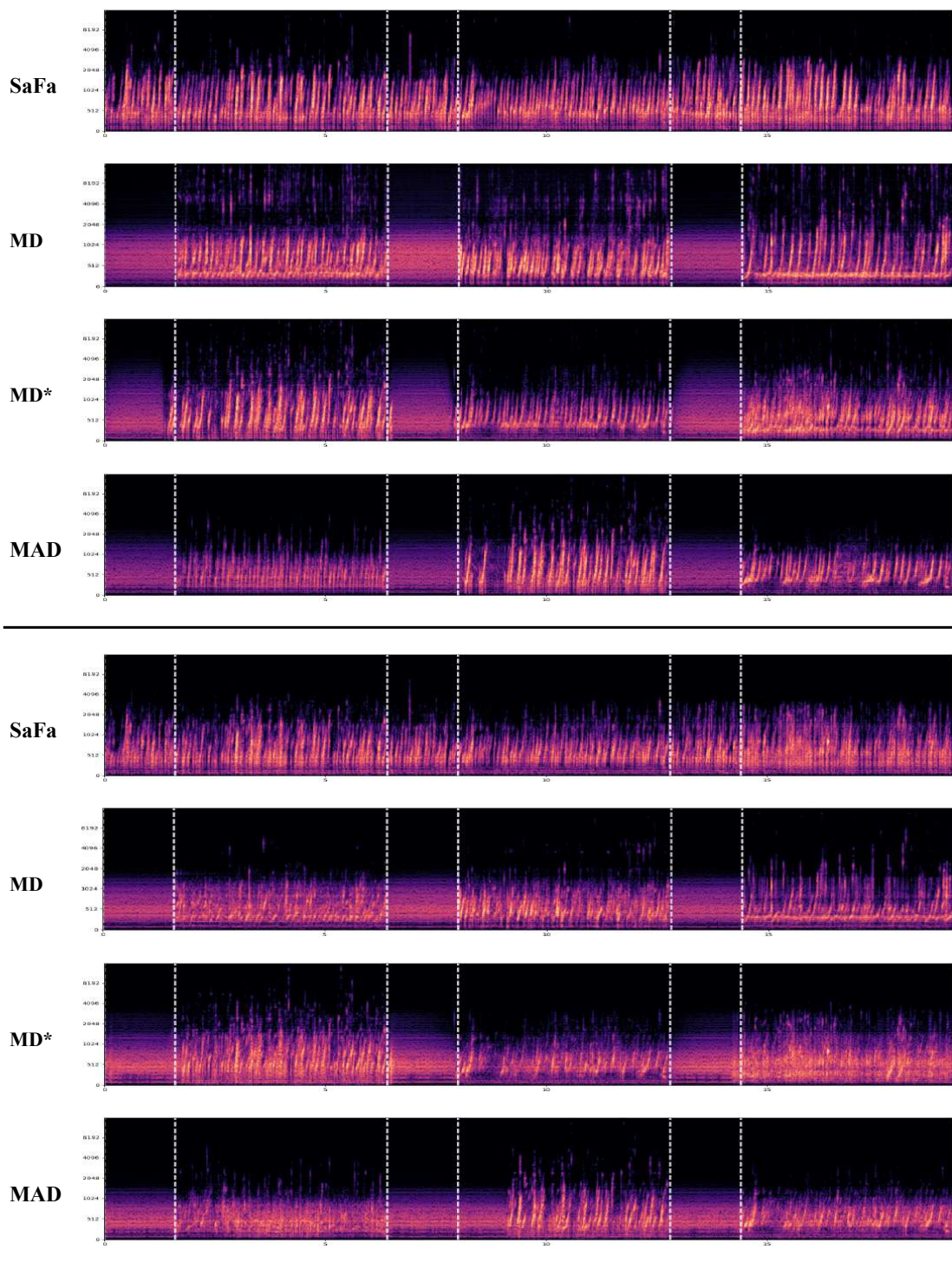


Figure 18. Qualitative comparison on audio effect generation. MD* represent an enhanced MD method with triangular windows.

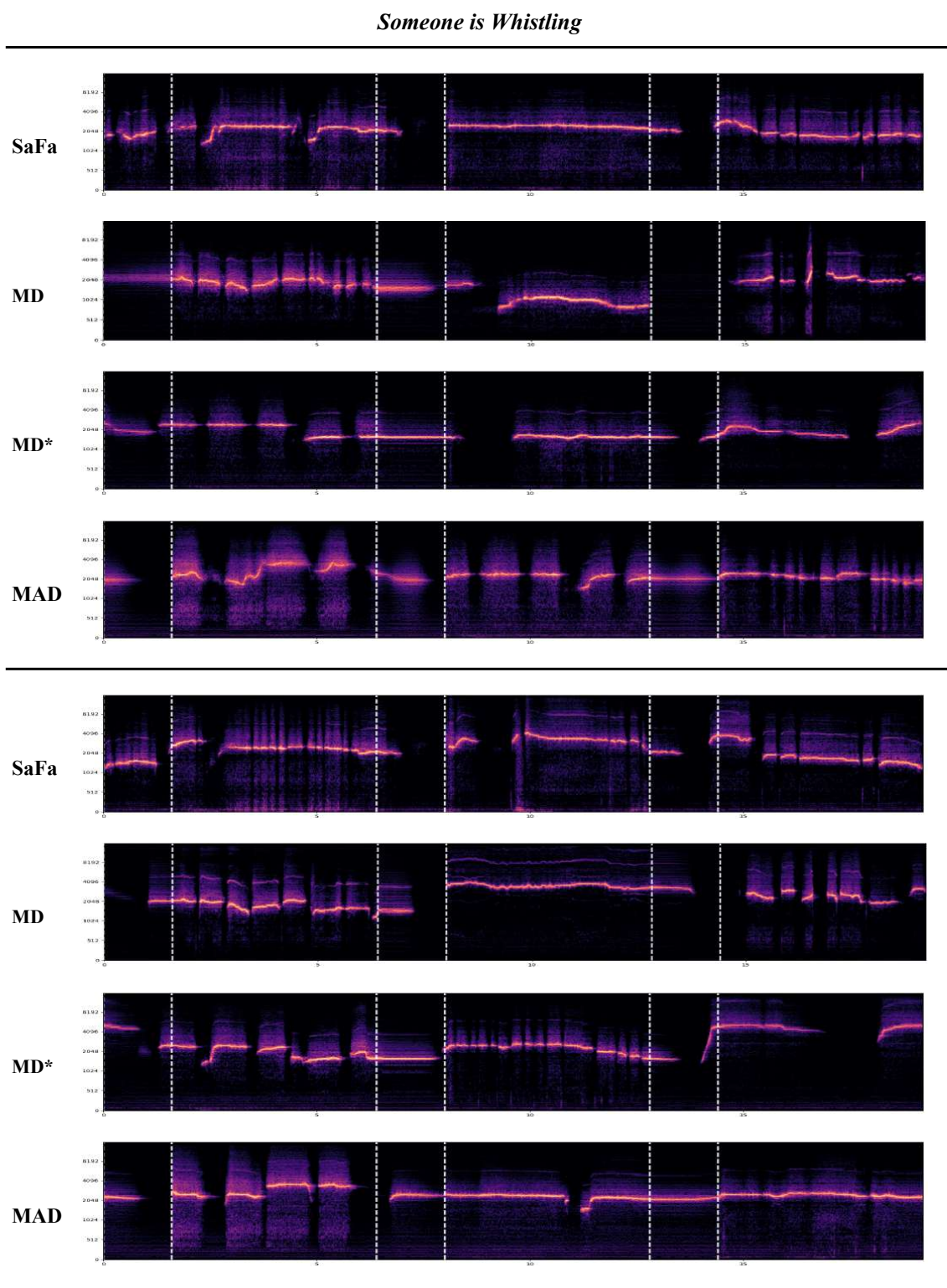


Figure 19. Qualitative comparison on audio effect generation. MD* represent an enhanced MD method with triangular windows.

The bell's sound is crisp and pleasant, with a distinct rhythm

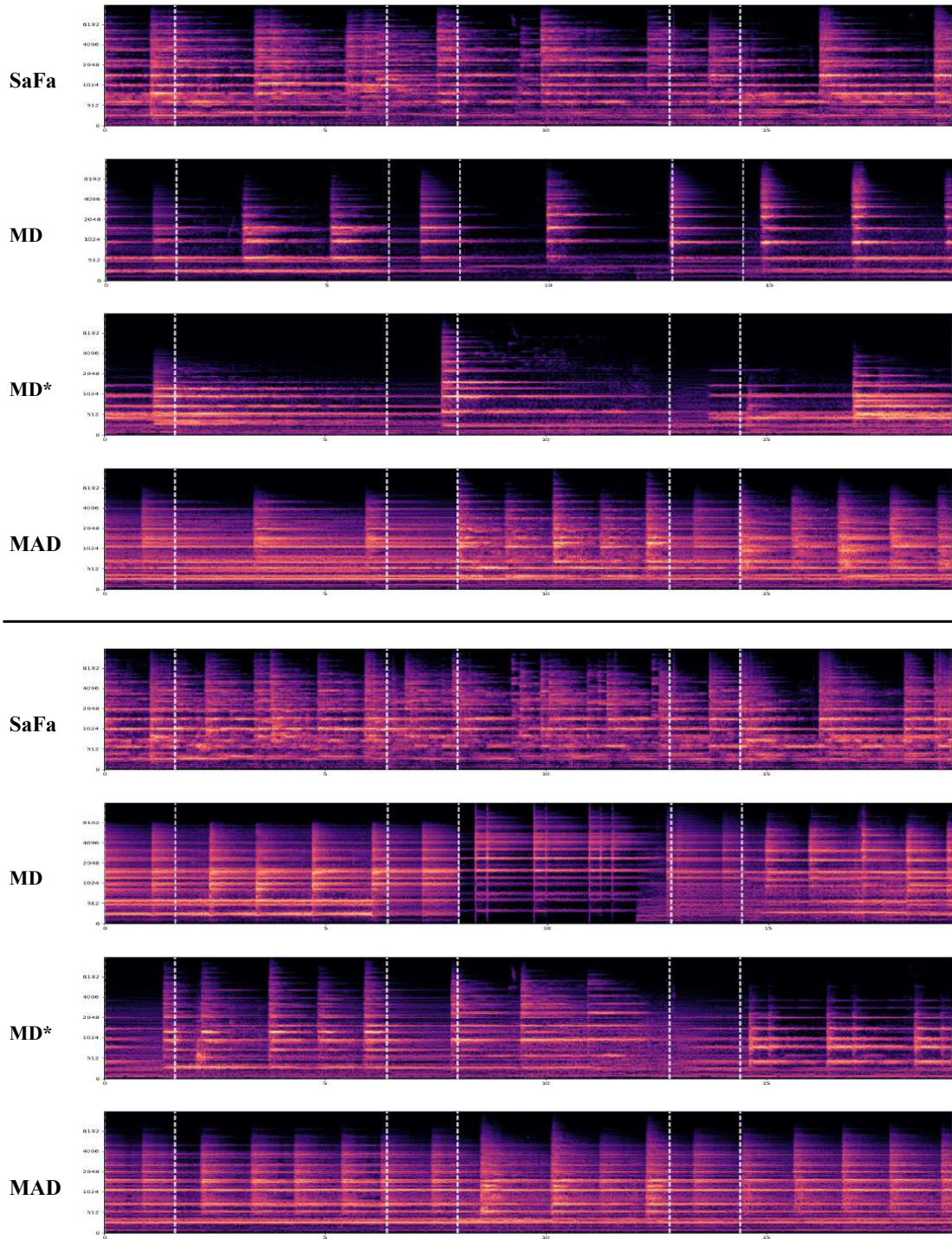


Figure 20. Qualitative comparison on audio effect generation. MD* represent an enhanced MD method with triangular windows.

A photo of a city skyline at night



Figure 21. Qualitative comparison on panorama image generation. MD* represent an enhanced MD method with triangular windows.

A photo of a forest with a misty fog

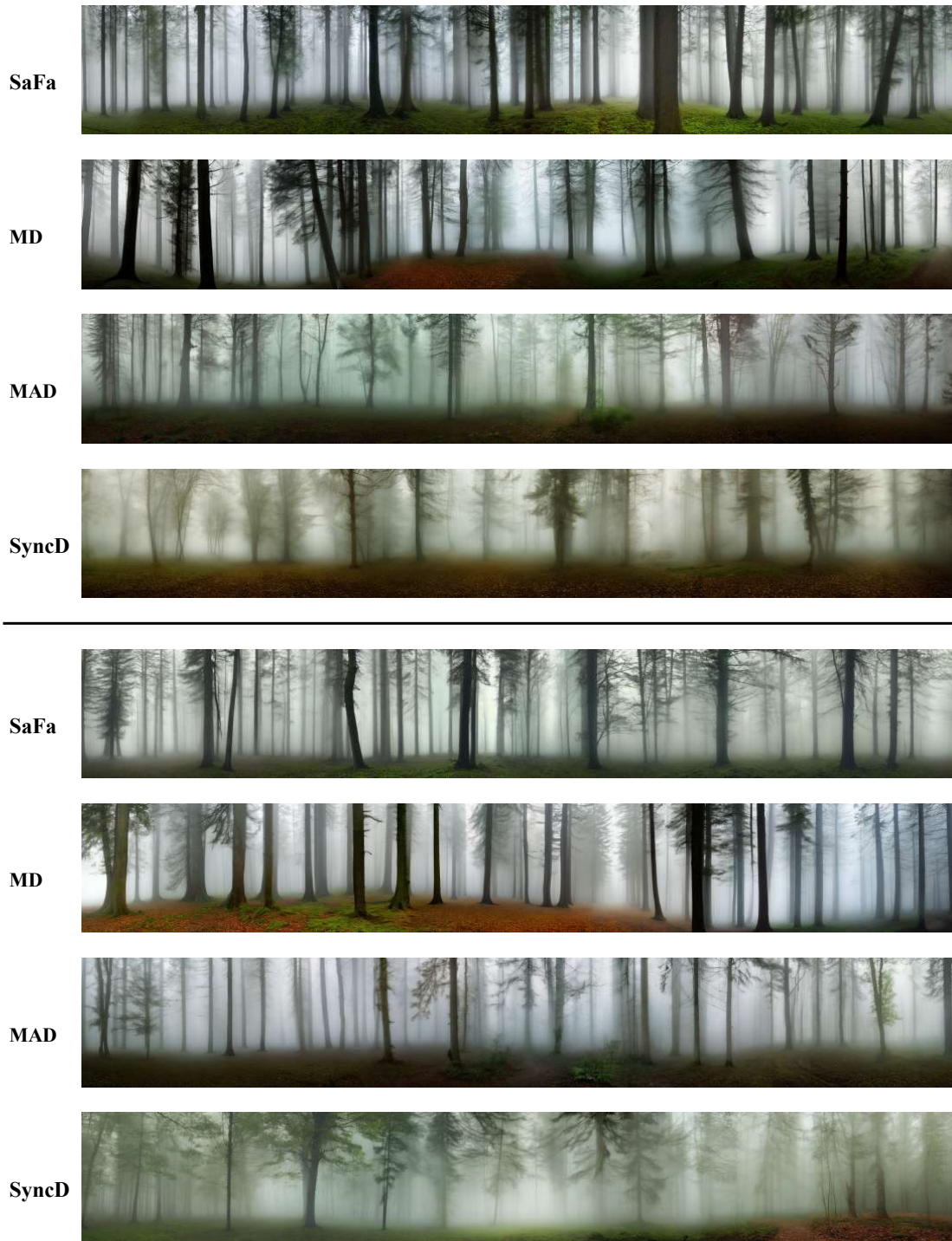


Figure 22. Qualitative comparison on panorama image generation. MD* represent an enhanced MD method with triangular windows.

A photo of a mountain range at twilight



Figure 23. Qualitative comparison on panorama image generation. MD* represent an enhanced MD method with triangular windows.

A photo of a snowy mountain peak with skiers

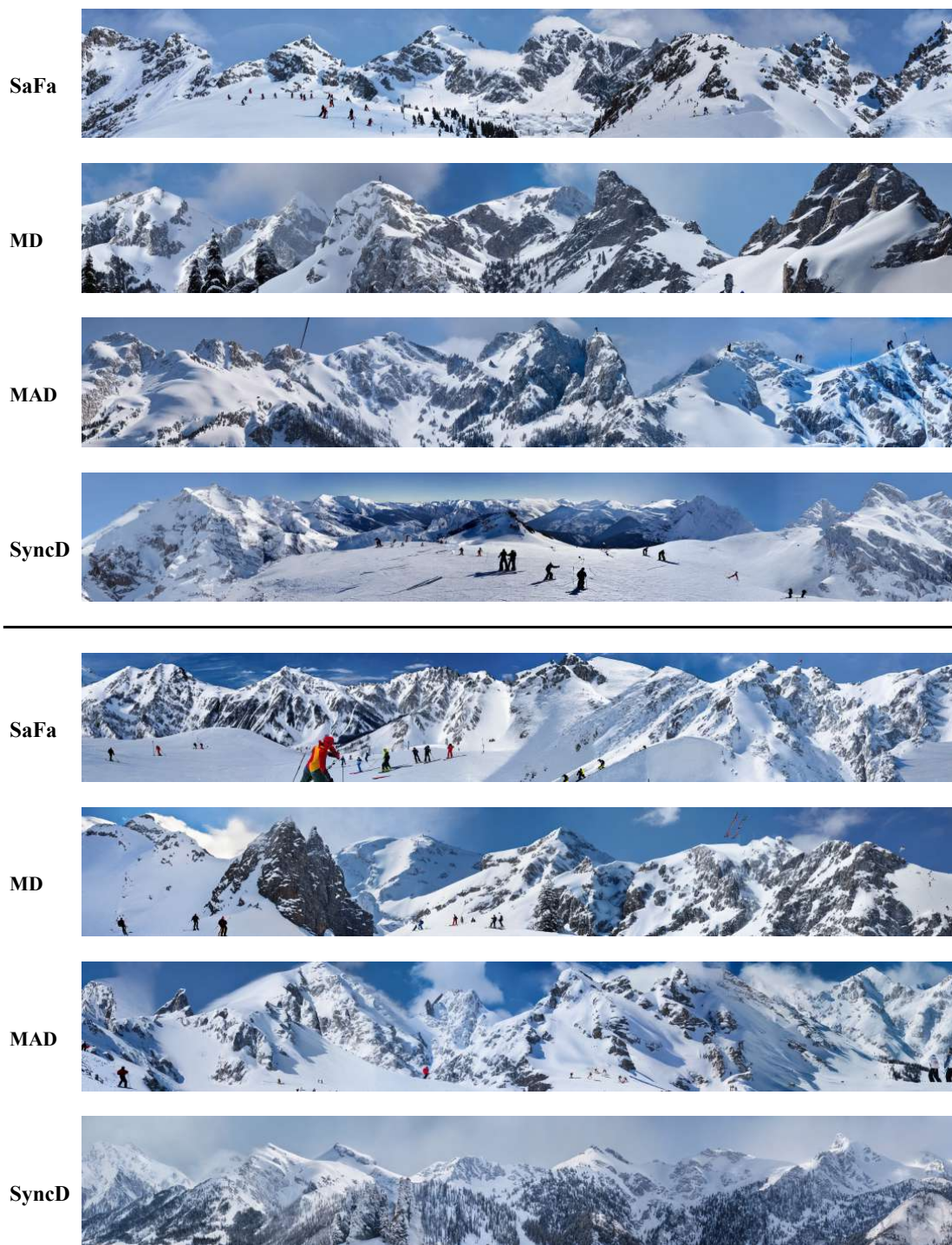


Figure 24. Qualitative comparison on panorama image generation. MD* represent an enhanced MD method with triangular windows.

Cartoon panorama of spring summer beautiful nature

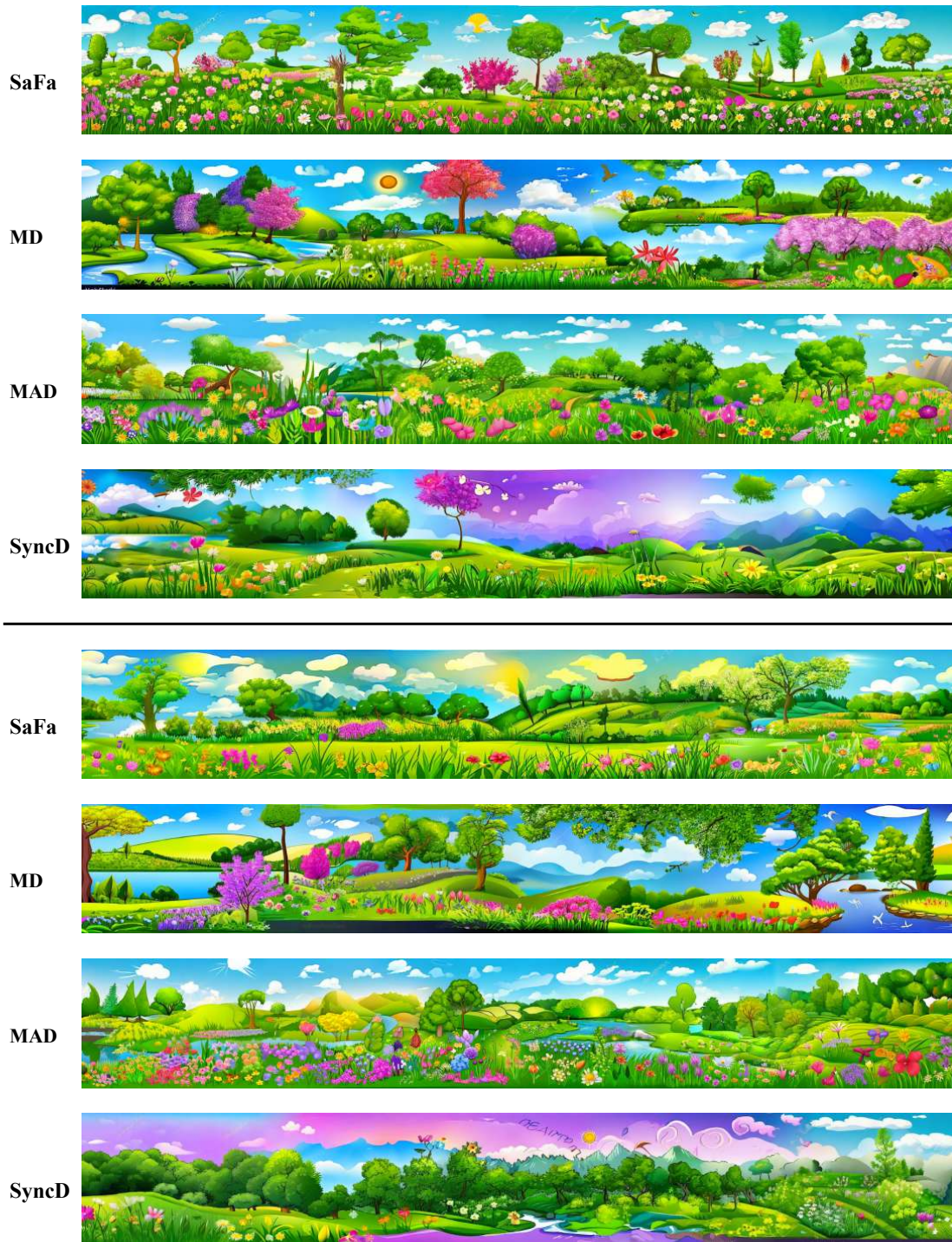


Figure 25. Qualitative comparison on panorama image generation. MD* represent an enhanced MD method with triangular windows.

Natural landscape in anime style illustration

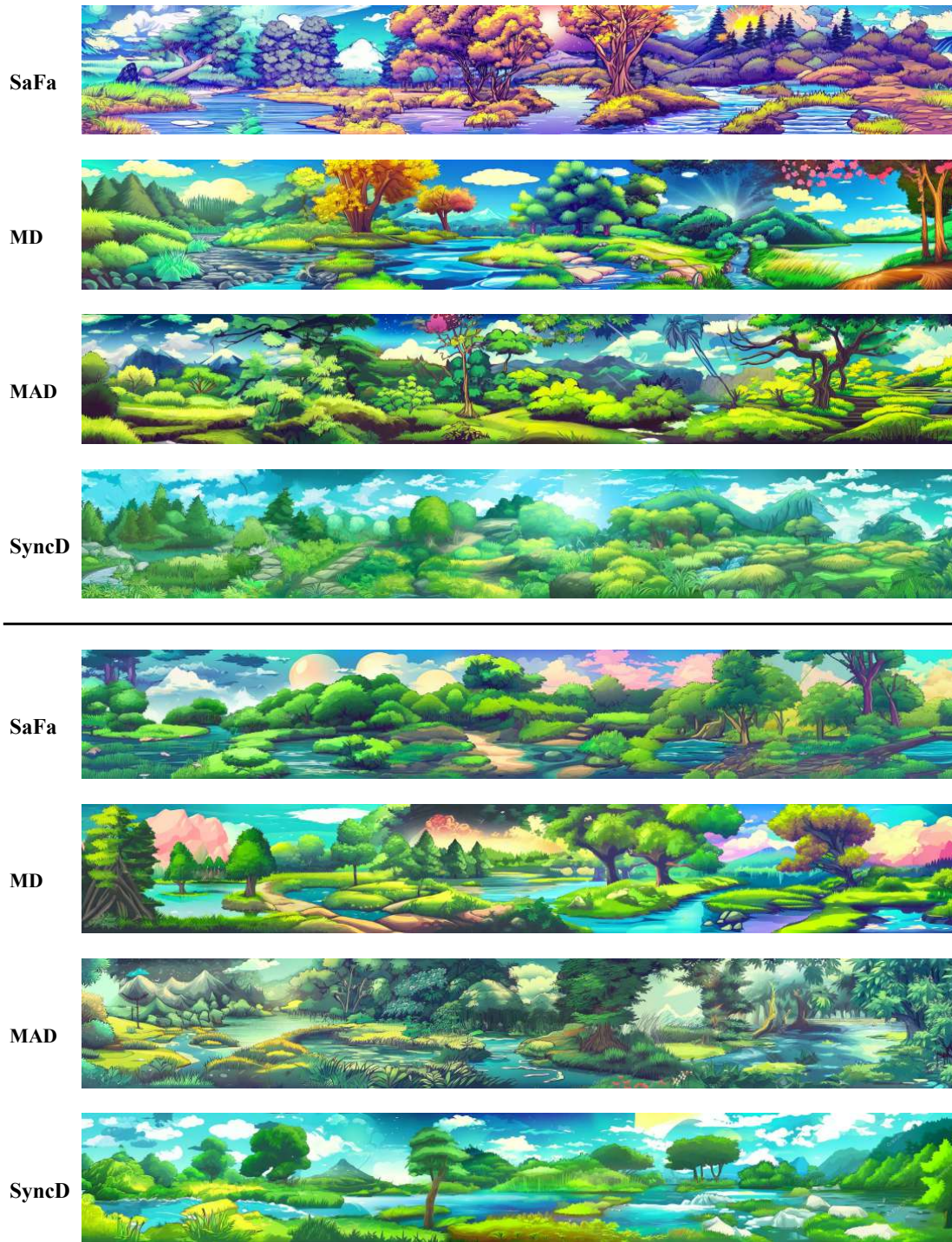


Figure 26. Qualitative comparison on panorama image generation. MD* represent an enhanced MD method with triangular windows.

A photo of a grassland with animals



A serene sunrise over a misty lake, with soft colors reflecting on the water's surface

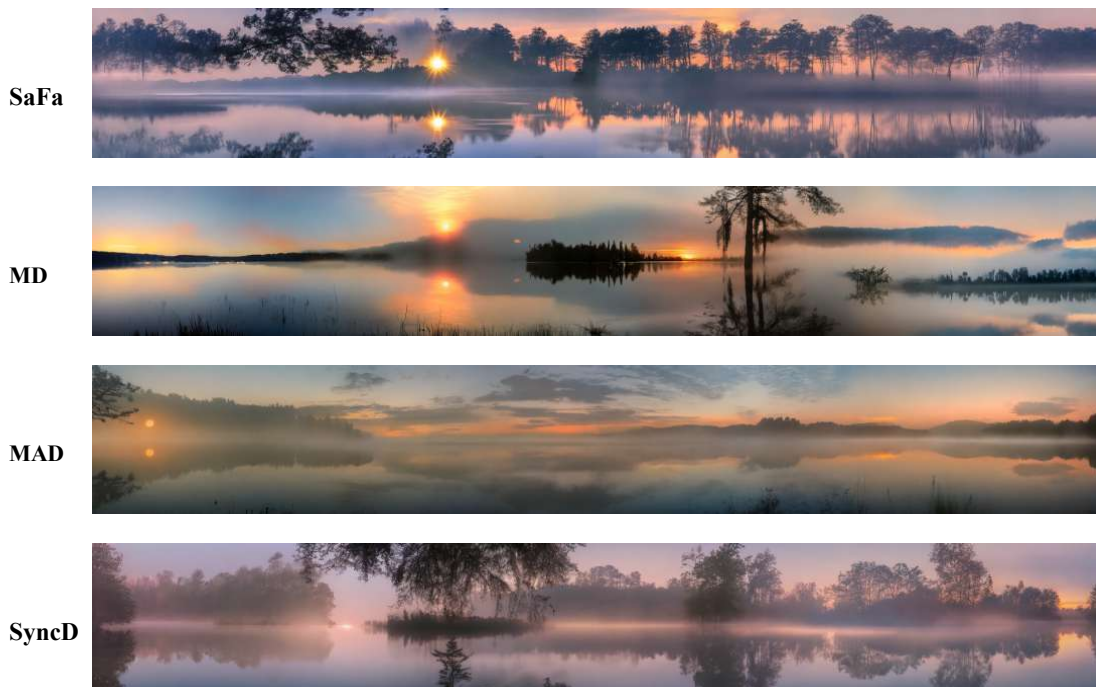
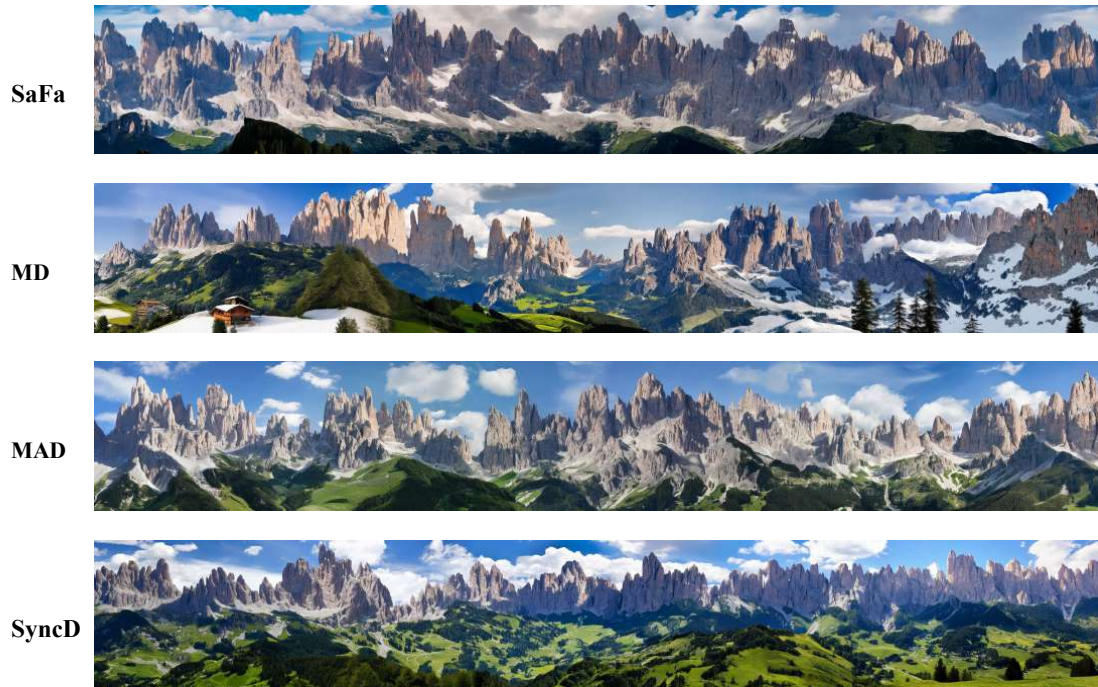


Figure 27. Qualitative comparison on panorama image generation. MD* represent an enhanced MD method with triangular windows.

A photo of the dolomites



A photo of a rock concert



Figure 28. Qualitative comparison on panorama image generation. MD* represent an enhanced MD method with triangular windows.

Create a vibrant landscape inspired by 'Qingming Riverside Scene, with riverside life, farmers, tourists, mountains, and traditional buildings



a photo of Chinese ink a vibrant landscape with farmers, tourists, mountains, traditional buildings and animal



Figure 29. Qualitative comparison on panorama image generation. MD* represent an enhanced MD method with triangular windows.

Majestic red rock formations glowing in the sunset

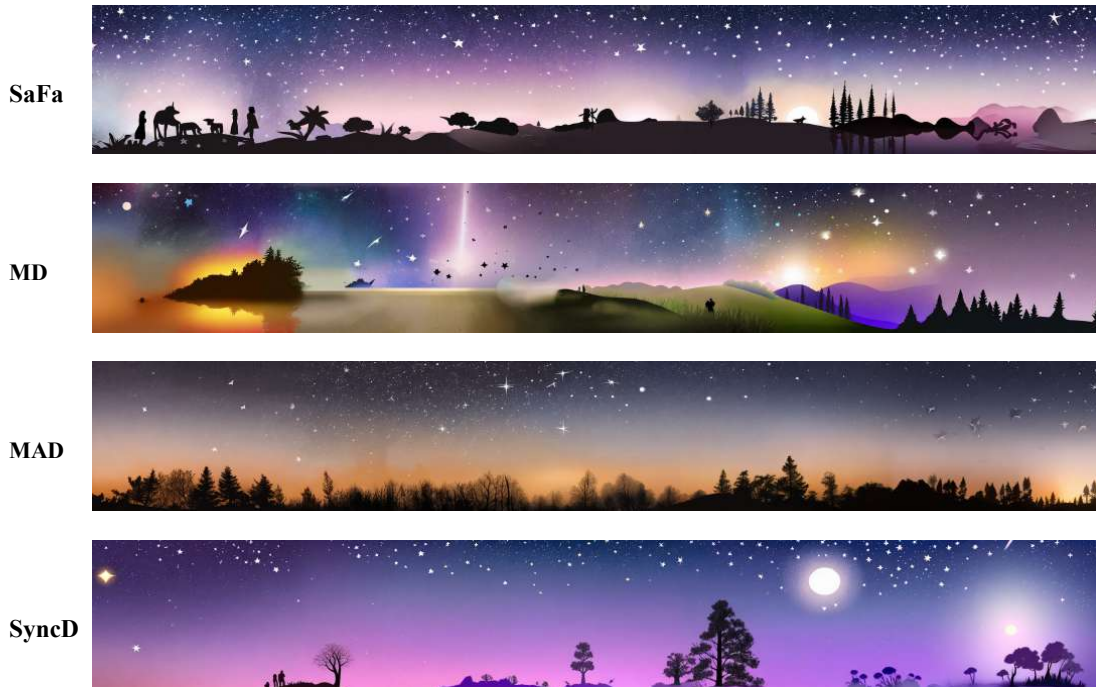


Serene mountain valley carpeted in vibrant fall foliage



Figure 30. Qualitative comparison on panorama image generation. MD* represent an enhanced MD method with triangular windows.

Silhouette wallpaper of a dreamy scene with shooting stars



Tranquil pond surrounded by autumn leaves

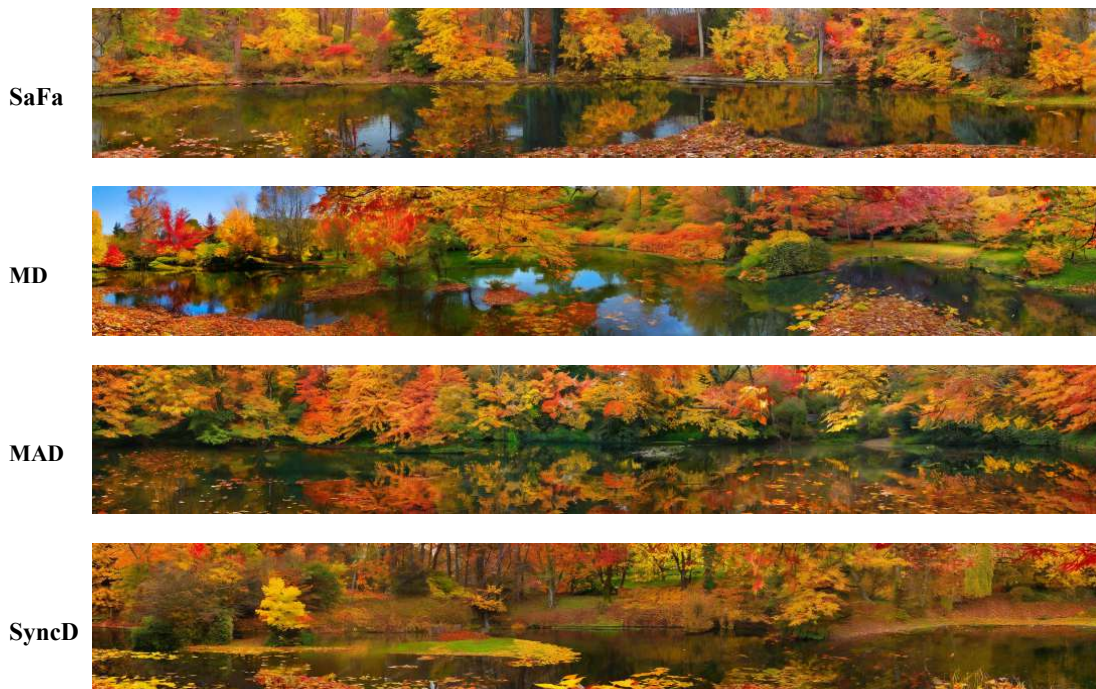


Figure 31. Qualitative comparison on panorama image generation. MD* represent an enhanced MD method with triangular windows.